

1 **Title:** Senescence rewires microenvironment sensing to facilitate anti-tumor immunity

2
3 **Running title:** Senescence enhances tumor cell sensitivity to host IFN- γ

4
5 **Authors:**

6 Hsuan-An Chen^{1,2}, Yu-Jui Ho^{1,#}, Riccardo Mezzadra^{1,#}, Jose M. Adrover³, Ryan Smolkin²,
7 Changyu Zhu¹, Katharina Woess⁴, Nicholas Bernstein⁵, Georgia Schmitt⁵, Linda Fong⁵, Wei
8 Luan¹, Alexandra Wuest¹, Sha Tian¹, Xiang Li¹, Caroline Broderick¹, Ronald C. Hendrickson⁶,
9 Mikala Egeblad², Zhenghao Chen⁵, Direna Alonso-Curbelo^{1,4,†}, Scott W. Lowe^{1,7,†}

10
11 **Affiliations:**

12 ¹ Department of Cancer Biology and Genetics, Memorial Sloan Kettering Cancer Center, New York,
13 NY 10065, USA

14 ² Louis V. Gerstner Jr Graduate School of Biomedical Sciences, Memorial Sloan Kettering Cancer
15 Center, New York, NY, USA

16 ³ Cold Spring Harbor Laboratory, Cold Spring Harbor, United States of America

17 ⁴ Institute for Research in Biomedicine (IRB Barcelona), The Barcelona Institute of Science and
18 Technology (BIST), Barcelona, Spain

19 ⁵ Calico Life Sciences, South San Francisco, CA, USA

20 ⁶ Microchemistry and Proteomics Core Laboratory, Memorial Sloan Kettering Cancer Center, New
21 York, NY 10065, USA

22 ⁷ Howard Hughes Medical Institute, Chevy Chase, MD 20815, USA

23 # These authors contributed equally to this work

24 † Corresponding Authors

25
26 **Corresponding authors:** Scott W. Lowe. Phone: 646-888-3342; Memorial Sloan Kettering
27 Cancer Center, 417 East 68th Street, 10065 New York, USA. E-mail: lowes@mskcc.org; and
28 Direna Alonso-Curbelo, Institute for Research in Biomedicine (IRB Barcelona), Carrer de Baldiri
29 Reixac, 10, 08028 Barcelona, Spain. Phone: 858-291-9384; E-mail: [direna.alonso-](mailto:direna.alonso-curbelo@irbbarcelona.org)
30 curbelo@irbbarcelona.org.

31
32 **Authors' Disclosures**

33 M. Egeblad is a member of the research advisory board for Brensocatib for Insmad, Inc, a
34 member of the scientific advisory board for Vividion Therapeutics, Inc., and a consultant for
35 Protalix, Inc. S.W. Lowe is a consultant and holds equity in Blueprint Medicines, ORIC
36 Pharmaceuticals, Mirimus Inc., PMV Pharmaceuticals, Faeth Therapeutics, and Constellation
37 Pharmaceuticals. No potential conflicts of interest were disclosed by the other authors.

38 **ABSTRACT**

39 Cellular senescence involves a stable cell cycle arrest coupled to a secretory program that, in
40 some instances, stimulates the immune clearance of senescent cells. Using an immune
41 competent liver cancer model in which senescence triggers CD8 T cell-mediated tumor rejection,
42 we show that senescence also remodels the cell surface proteome to alter how tumor cells
43 sense environmental factors, as exemplified by Type II interferon (IFN- γ). Compared to
44 proliferating cells, senescent cells upregulate the IFN- γ receptor, become hypersensitized to
45 microenvironmental IFN- γ , and more robustly induce the antigen presenting machinery—effects
46 also recapitulated in human tumor cells undergoing therapy-induced senescence. Disruption of
47 IFN- γ sensing in senescent cells blunts their immune-mediated clearance without disabling the
48 senescence state or its characteristic secretory program. Our results demonstrate that
49 senescent cells have an enhanced ability to both send and receive environmental signals, and
50 imply that each process is required for their effective immune surveillance.

51

52 **SIGNIFICANCE**

53 Our work uncovers an interplay between tissue remodeling and tissue sensing programs can be
54 engaged by senescence in advanced cancers to render tumor cells more visible to the adaptive
55 immune system. This new facet of senescence establishes reciprocal heterotypic signaling
56 interactions that can be induced therapeutically to enhance anti-tumor immunity.

57

58

59 INTRODUCTION

60 Cellular senescence is a stress response program characterized by a stable cell cycle
61 arrest and a secretory program capable of remodeling the tissue environment (1). In normal
62 tissues, senescence contributes to tissue homeostasis during wound healing; however, in aged
63 or damaged tissues, the aberrant accumulation of senescent cells can cause chronic
64 inflammation and reduced tissue regenerative capacity (2-4). In cancer, senescence has been
65 shown to mediate both beneficial and detrimental effects on tissue biology. On one hand,
66 senescence provides a barrier to oncogene-initiated tumorigenesis and contributes to the anti-
67 tumor activity of some cancer therapies (5,6). On the other, the persistence of senescent tumor
68 cells post therapy can produce a tissue environment that promotes relapse and metastasis (7,8).
69 The molecular underpinnings of these opposing biological outputs remain poorly understood.

70 One facet of the senescence program that is likely to contribute to such diverse biology
71 is the senescence-associated secretory phenotype [SASP; ref. (9)]. SASP is activated through a
72 global chromatin remodeling process that evolves over time and is controlled by key epigenetic
73 regulators such as BRD4 and pro-inflammatory transcription factors such as NF- κ B and C/EBP-
74 β (10-12). This, in turn, leads to the induction of genes that encode tissue remodeling proteins
75 such as matrix metalloproteinases, growth factors, and fibrolytic factors known to play crucial
76 roles in wound healing process (3,13,14). Other SASP components include chemokines and
77 cytokines that can alter the composition and state of immune cells within the tissue, leading to
78 the immune-mediated targeting and clearance of the senescent cells themselves (15,16).
79 Nonetheless, the aberrant accumulation of senescent cells in many pathological contexts
80 implies that immune mediated clearance is not a universal outcome of senescence or the SASP
81 and raises the possibility that additional mechanisms dictate the paradoxically beneficial and
82 detrimental effects of senescence in tissue biology and immune surveillance (17-19).

83 Certainly, senescence-associated immune surveillance can have potent anti-cancer
84 effects, though the precise effector mechanisms vary with tissue and cell type (10,15,16,20). In
85 mouse models of hepatocellular carcinoma (HCC), liver tumor cells triggered to senesce are
86 eliminated by immune-dependent mechanisms engaged by wild-type p53 (15). In agreement,
87 *TP53* is frequently mutated in human HCC, particularly in the “Proliferation class” tumors
88 showing the worst prognosis (21,22). Though immunotherapy and TP53-targeting drugs are
89 emerging as promising strategies to improve disease outcomes, the molecular basis for
90 response and resistance remains unknown (23-25). Therefore, understanding the mechanisms
91 by which senescent liver tumor cells become visible to the immune system may facilitate
92 strategies to elicit anti-tumor immunity in *TP53*-mutated HCC that may extend to other tumor
93 types.

94 Here, we set out to establish principles that modulate the immune recognition and
95 clearance of senescent cells to identify actionable senescence mechanisms that may be
96 exploited to improve the immune control of cancer. To this end, we developed a novel
97 ‘senescence-inducible’ model in which liver cancer cells can be selectively switched to a
98 senescent state through genetic modulation of endogenous p53. We reasoned this would mimic
99 the effects of therapies that trigger senescence (26,27) while avoiding the confounding effects of
100 senescence-inducing therapies on immune cells or other components of the tissue environment.
101 Using this model and then extending to other systems, we reveal that, in addition to the SASP,
102 senescence drives a major remodeling of the cell surface proteome and signaling programs in a
103 manner predicted to fundamentally alter the way cells sense and respond to environmental
104 signals, exemplified herein through a hypersensitivity to microenvironmental type II IFN (IFN- γ).
105 This process enables a more robust upregulation of the antigen processing and presenting
106 machinery in senescent tumor cells that renders them susceptible to immune surveillance *in*
107 *vivo*. Thus, our results reveal a rewired tissue-sensing program in senescent cells that acts in

108 concert with SASP to boost their immunogenic potential, thereby facilitating immune-mediated
109 tumor rejection.

110

111 **RESULTS**

112 **A p53-restorable immunocompetent tumor model to study senescence surveillance**

113 To study how senescence reprograms cellular and tissue states, we exploited
114 hydrodynamic tail vein injection (HTVI) technique (28) to generate a senescence-inducible liver
115 cancer model controlled by a tumor-specific, restorable p53 short-hairpin RNA (shRNA).
116 Specifically, adult liver hepatocytes of immunocompetent Bl/6 mice were transfected *in vivo* with
117 a sleeping beauty SB13 transposase vector and two transposon constructs (encoding
118 NrasG12D-IRES-rtTA and TRE-tRFP-shp53, or “NSP”) which integrate in the genome. In this
119 Tet-On system, endogenous p53 is suppressed in the presence of doxycycline (Dox) through
120 the activation of inducible shRNA linked to RFP (**Fig. 1A**), enabling genetic control of
121 senescence in established tumors. Consistent with the co-occurrence of mutations that
122 inactivate *TP53* and activate cell proliferation signaling pathways (e.g. PI3K/AKT and
123 RAS/MAPK cascades) in human liver tumors, the cooperation between oncogenic RAS and
124 suppression of p53 led to hepatocyte transformation, with most mice developing tumors with
125 poorly differentiated features 5-8 weeks after HTVI. Transcriptional profiling revealed that these
126 murine tumors resemble the ‘Proliferation’ class of human HCC (Supplementary Fig. S1A-S1F),
127 which is the typical class of human HCC harboring *TP53* mutations (21,22,29).

128 Based on previous work (15), we anticipated that p53 reactivation in the above system
129 would trigger senescence and engage anti-tumor immunity. Accordingly, Dox withdrawal
130 triggered dramatic tumor regressions over the course of several weeks, leading to prolonged
131 animal survival (**Fig. 1B and 1C**). Analysis of the tumors at 14 days post Dox withdrawal
132 revealed the expected downregulation of the p53-shRNA (as visualized by the linked RFP

133 reporter) and accumulation of senescence-associated- β -galactosidase (SA- β -gal) without any
134 notable effects on the RAS-effector p-ERK (**Fig. 1D**). Similarly, an increase in SA- β -gal activity
135 and SASP-associated transcriptional profiles, together with a concomitant proliferative arrest,
136 were observed in explanted tumor cells 6-8 days following p53 restoration (Supplementary Fig.
137 S2A-S2H). Of note, engraftment of these cultures (kept on Dox to maintain p53 silencing) into
138 Dox-fed immunocompetent mice produced synchronous and focal secondary tumors that
139 regressed with similar kinetics as the primary tumors upon Dox withdrawal (**Fig. 1B**;
140 Supplementary Fig. S3A-S3E). Control experiments using a Tet-Off system or incorporating a
141 constitutive p53 shRNA ruled out the possibility that Dox itself had any effect on tumor behavior
142 in our model (Supplementary Fig. S3F and S3G). Therefore, this system allows for the efficient
143 induction of senescence in tumor cells without resorting to therapies that can also alter the host
144 immune system. Given its added flexibility, we used the orthotopic transplant model (hereafter
145 referred to as 'NSP') for many of the mechanistic studies described below.

146 As anticipated, the marked tumor regressions noted above were immune mediated.
147 Hence, NSP tumors that arose following transplantation into immunocompromised Nude and
148 *Rag2^{-/-}Il2rg^{-/-}* (R2G2) mice underwent a prominent cytostatic response but failed to regress, with
149 R2G2 animals showing the most profound defects (**Fig. 1E-1G**; Supplementary Fig. S3H and
150 S3I). As Nude mice are defective in adaptive immunity whereas R2G2 are also compromised
151 for aspects of innate immunity, these results imply that the adaptive immune system is essential
152 for efficient tumor regression in the model and establish a well-controlled experimental context
153 to explore the mechanistic basis for these effects.

154 **Senescence triggers a switch from tumor immune evasion to immune recognition**

155 To characterize the tumor suppressive paracrine effects of senescence, we next
156 characterized the immune microenvironments of tumors harboring p53-suppressed (referred to
157 as "proliferating") and p53-restored (referred to as "senescent") tumor cells after one week of

158 Dox withdrawal, a time when senescence is established but tumors have not yet regressed
159 (Supplementary Fig. S4A; Fig. S2-S3). Lesions harboring senescent tumor cells showed a ~1.8-
160 fold increase in total CD45+ immune cells compared to proliferating controls [Fig. 2A; refs.
161 (15,16)]. Immunophenotypic and histologic analyses (at day 9 post-Dox withdrawal) revealed
162 that this involved a prominent increase in the percentage of lymphocytes (B cells, CD4+ and
163 CD8+ T cells) and a decrease in the percentage of Gr-1+ myeloid-derived suppressor
164 cells/neutrophils (CD11b+Gr1+Ly6C low) (Fig. 2B; Supplementary Figs. S4B). While the
165 fraction of macrophages as a percentage of total CD45 population remained unchanged, the
166 absolute numbers were markedly increased (Fig. 2A and 2B; Supplementary Fig. S4C-S4E).
167 Within the T cell population, accumulating CD8 T cells showed markers of antigen experience
168 (CD44+, CD69+) and harbored an increased population of effector cells (CD44+CD62L-) [Fig.
169 2C; ref. (30)]. This overall remodeling of immune environment led to a significant increase in the
170 CD3:neutrophil ratio for tumors harboring senescent cells (Supplementary Fig. S4F), effects
171 consistent with similar increases in the CD3:neutrophil ratio which have been associated with
172 immune reactivity in human liver tumors (31). The remodeling could be clearly visualized using
173 three dimensional (3D) imaging after tissue clearing [Fig. 2D; Supplementary Fig. S4G and S4H;
174 Supplementary video S1; ref. (32)].

175 To pinpoint the specific immune cell types responsible for immune surveillance of
176 senescent tumor cells, we generated parallel cohorts of mice harboring orthotopic NSP tumors
177 and examined the impact of depleting various immune cell populations on tumor regressions
178 after Dox withdrawal. Whereas blocking antibodies targeting neutrophils/monocytes (Gr1), NK
179 cells (NK1.1), and CD4+ T cells (GK1.5) had no effect, depletion of CD8+ T cells (2.43) and
180 macrophages (using liposomal clodronate which selectively targets macrophages
181 (CD11b+F4/80+) but not cDC (CD11b-CD11c+MHC-II+CD103+); ref. (33,34)) markedly
182 impaired tumor regression (Fig. 2E; Supplementary Fig. S4I).

183 To characterize how p53-driven tumor senescence results in productive anti-tumor
184 immunity, we performed single-cell RNA-seq (scRNA-seq) analysis of freshly isolated CD45
185 cells from proliferating and senescent NSP tumors early after Dox withdrawal (8 days)
186 (Supplementary Fig. S5A and S5B), and used the differential abundance testing algorithm Milo
187 (35) to capture cell state shifts within the immune cell types mediating this process
188 (Supplementary Fig. S5C-S5F). In line with their contribution to tumor regression, the CD8+ T
189 cell and macrophage subpopulations showed marked changes in quantity and state.
190 Concerning T cells, proliferating (p53-suppressed) tumors were significantly enriched in CD8+ T
191 states exhibiting high expression of both dysfunction markers (*Tox*, *Tigit*, *Lag3*, *Ctla4*,
192 *Pdcd1/CD137*, *Cd160*) and activation markers (*Prf1*) (Figs. 2F and 2G; Supplementary Fig. S5G,
193 Supplementary Table S1). These CD8+ T cells also showed high levels of *Tnfrsf9*, a marker
194 known to delineate T cells subsets that have the capacity to become reinvigorated in human
195 HCC and other cancer types (36,37). In stark contrast, in senescent (p53-reactivated) lesions,
196 CD8 T populations appeared highly activated, showing low levels of dysfunction markers and
197 high expression of effector cytokines (e.g. *Ifng*, *Tnf*, Supplementary Table S1). Accordingly,
198 transcriptional profiling of bulk tumor tissues showed immune active and cytotoxic signatures in
199 senescent tumors undergoing regression [Supplementary Fig. S5H; ref. (38)].

200 Changes to the macrophage compartment provided further evidence that tumor cell
201 senescence triggered an immune evasion-to-surveillance switch. Hence, scRNA-seq,
202 immunophenotyping and histology indicated that tumor-associated macrophage phenotypes
203 transitioned from F4/80^{low};CD11c^{high} states (cluster 8), including immune-suppressive PDL1+
204 populations (characteristic of human HCC tumors with poor prognosis (39,40)), to
205 F4/80^{high};CD11c⁻ states (cluster 0), defined by high expression of an antigen-presentation gene
206 signature (Supplementary Figs. S5E-S5J; S6A and S6B; Supplementary Table S1). Of note,
207 these senescence-associated F4/80^{high};CD11c⁻ macrophages were particularly sensitive to the
208 liposomal clodronate treatment (Supplementary Fig. S6C-S6E), which also resulted in a

209 significant reduction in the fraction of active CD8 but not CD4 T cells (Supplementary Fig. S6F
210 and S6G), indicating a CD8-dependent immune response involving cooperativity with
211 macrophages. Accordingly, histological analyses confirmed that accumulating CD8+ T cells and
212 F4/80+ macrophages were frequently co-enriched following senescence induction in tumors
213 (**Fig. 2H**; Supplementary Fig. S4D). Collectively, these biological and molecular analyses
214 support a model where tumor cell senescence induces an abrupt switch from immune evasion
215 to immune surveillance mediated by changes in macrophages and CD8+ T cell states, leading
216 to productive anti-tumor immunity and, ultimately, tumor rejection.

217

218 **Senescence remodels tissue sensing programs and cell-surfaceome landscape**

219 We next set out to exploit the above model to understand the molecular mechanisms
220 responsible for rendering senescent tumor cells visible to the immune system. Senescence
221 induction involves a chromatin remodeling program that silences proliferative genes and
222 activates many genes encoding SASP factors, with the latter program being largely dependent
223 on the enhancer reader, BRD4 (10). We therefore performed transcriptional profiling
224 experiments on NSP cells under proliferating (p53-suppressed) versus senescent (p53-restored)
225 conditions in the absence and presence of JQ1, a drug that inhibits BRD4 function
226 (Supplementary Table S2). Consistent with expectations, p53 restoration dramatically reduced
227 the expression of proliferative genes and induced the expression of well-known SASP factors
228 [**Fig. 3A**; Supplementary Fig. S7A; ref. (7)], including several cytokines known to stimulate T
229 cells (*Cxcl16*, *Il18*) or macrophage activation and recruitment (*Csf2*, encoding protein GM-CSF)
230 or previously linked to senescence (*Igfbp7*, *Igfbp3*, *Pdgfa*). As anticipated from previous work
231 (10), many of the upregulated SASP-encoding transcripts (~65%) were BRD4-dependent
232 (Supplementary Fig. S7B). Similarly, a range of growth factors and immune modulators were
233 secreted from the senescent cells as assessed by multiplexed cytokine assays, including the T
234 cell and macrophage attractants CCL5, CXCL9, and GM-CSF as well as the vasculature

235 remodeling factor VEGF (Supplementary Fig. S7C). Therefore, senescence in p53-restored
236 NSP tumor cells is associated with a robust SASP, consistent with the marked remodeling of the
237 immune ecosystem characterized above.

238 Strikingly, examination of the subcellular localization for differentially expressed genes
239 (DEGs) revealed that senescent tumor cells not only increased their expression of secreted
240 ('extracellular', EC) SASP factors, but also displayed major changes in the expression levels of
241 transcripts encoding surface proteins ('plasma membrane', PM) (**Fig. 3B**). Indeed, 25% of total
242 upregulated DEGs encoded PM proteins, a significant enrichment that deviated from the
243 random distribution (15%) (**Fig. 3B**). Dynamic PM-DEGs were linked to protein tyrosine kinase
244 signaling transduction (*Nrp1*, *Egfr*), cytokine receptor activity (*Ifngr1*), ECM receptors (*Itgb3*,
245 *Cd44*) and ion transporters (*Slc12a1*, *Slc24a3*) and captured known senescence-associated
246 molecules (*Cd44*, *Vcam1*, and *Itgb3*), suggesting senescent cells may have an enhanced
247 capability to interact with and sense their environment [**Fig. 3C**; Supplementary Fig. S7D; refs.
248 (41-43)].

249 Interestingly, the senescence-associated increase in the expression of many of these
250 PM proteins was blunted by JQ1, suggesting that their induction may be part of the broader
251 chromatin remodeling program coupled to SASP [**Fig. 3D**; ref. (10)]. Of note, profound changes
252 in the transcription of genes encoding PM proteins also occurred in p53-deficient NSP tumor
253 cells treated with the senescence-inducing drug combination trametinib and palbociclib
254 [Supplementary Fig. S7E-top panel; Supplementary Table S2; ref. (20)] and in a series of 13
255 genetically-diverse *TP53* wild-type and *TP53* mutant human cancer lines—derived from liver,
256 breast, lung, and colon cancers induced to senesce by various triggers [**Fig. 3E**; Supplementary
257 Fig. S7F; ref. (44)] This was particularly robust for upregulated (but not downregulated) PM-
258 DEGs, reminiscent of effects observed for extracellular (EC) SASP factors (**Fig. 3E**;
259 Supplementary Fig. S7E-bottom panel). Therefore, the markedly altered expression of cell

260 surface proteins we observed in our model extends beyond p53-induced senescence and may
261 be a hallmark of the senescent state.

262 To validate the global remodeling of PM factors in senescence at the protein level, we
263 performed surface proteomics on isogenic proliferating and senescent NSP tumor cells, using a
264 biotin-labeling enrichment method, where cell surface proteins were labeled with membrane-
265 impermeable biotin, purified, and subjected to mass spectrometry [Fig. 3F; Supplementary Fig.
266 S7G; ref. (45)]. A strong correlation between biological replicates under each condition was
267 observed (Supplementary Fig. S7H), with detected proteins being enriched for annotated
268 plasma membrane proteins by 60% after induction of p53-induced senescence. Of 887 proteins
269 that were reproducibly detected, more than 50 % were differentially expressed. Most
270 differentially expressed proteins correlated well with the directionality observed in our
271 transcriptional profiling data, although some were differentially expressed without a
272 corresponding change in transcript levels (Supplementary Fig. S7I).

273 Annotated cell surface proteins detected by mass spectrometry upon senescence
274 induction included several previously linked to senescence (e.g. CD44, VCAM1), various growth
275 factor and cytokine receptors (e.g. EGFR, ICAM1 and IFNGR1), and other, less characterized
276 factors (Fig. 3F-3H; Supplementary Fig. S7J and S7K). Of note, the set of cell surface-enriched
277 proteins identified in our model showed limited overlap with those identified in human fibroblasts
278 undergoing oncogene-induced senescence (46), suggesting heterogeneity between cell types
279 or senescence triggers. Regardless, these results show that in addition to a rewiring in their
280 secretory program, senescent cells undergo profound changes in the content and abundance of
281 cell surface proteins, and imply that senescent cells acquire distinctive microenvironment-
282 sensing traits that may influence their state and fate in vivo.

283

284 **Senescent cells are primed to sense IFN- γ and amplify IFN- γ signaling**

285 To identify pathways that might functionally influence how senescent cells sense their
286 environment, we mined transcriptional and proteomic datasets for senescence-associated
287 changes linked to anti-tumor immunity. Interestingly, GO analysis revealed that Type II
288 interferon-gamma (IFN- γ) response (47) was among the top 5 annotated pathways enriched
289 during senescence and dependent on cell state-specific enhancer programs (i.e. JQ1-sensitive;
290 i.e. "C1" of Fig. 3D) (Supplementary Fig. S8A). Among the altered transcripts, we noted several
291 positive regulators of IFN- γ signaling, including the IFN- γ receptor subunit IFNGR1 (one of the
292 most significantly upregulated proteins from our proteomic data) and multiple interferon effectors
293 [*Irf1*, *Irf7* and *Irf9*; refs. (47,48)] (**Fig. 4A-4C**; Supplementary Fig. S8B and S8C). Besides these
294 Brd4-sensitive upregulated genes, transcripts encoding negative regulators of IFN- γ signaling
295 (*Ptpn2*, *Socs1* and *Socs3*) were significantly decreased [**Fig. 4C**; refs. (49,50)]. Similar changes
296 were noted in NSP tumor cells treated with different senescence inducers (**Fig. 4C**;
297 Supplementary Fig. S8D-S8G) and, more broadly, in a panel of 13 human breast, lung, liver and
298 colon derived cancer cell lines triggered to senesce [**Fig. 4D**; ref. (44)]. Therefore, changes in
299 the expression of Type II IFN signaling components are a general feature of senescent cells,
300 independent of cell type, cell genotype, species, and nature of the senescence inducer.

301 The concurrent increase in IFN- γ signaling effectors and decrease in negative regulators
302 led us to hypothesize that senescent cells become primed to sense IFN- γ within their
303 environment. To test this hypothesis directly, we treated proliferating and senescent NSP cells
304 with recombinant IFN- γ and performed immunoblotting analyses of JAK-STAT signaling
305 activation. While IFN- γ dramatically increased the baseline levels of STAT1 in both states,
306 senescent cells accumulated more phosphorylated STAT1, irrespective of the senescence
307 trigger (**Fig. 4E**; Supplementary Fig. S8H). Additionally, we also found an increased level of
308 phosphorylated JAK1 in p53-restored senescent cells, further supporting our finding on a more
309 active JAK-STAT signaling pathway in senescent cells sensing IFN- γ (Supplementary Fig. S8I).

310 As predicted from transcriptional analyses, senescence also triggered a decrease in PTPN2
311 protein (51), irrespective of the presence of exogenous IFN- γ (**Fig. 4E**). Thus, senescent cells
312 more efficiently activate IFN- γ signaling in response to limiting concentration of IFN- γ in the
313 environment.

314

315 **Senescence and extracellular IFN- γ cooperatively upregulate the antigen processing and** 316 **presentation machinery**

317 To better understand the functional contribution of IFN- γ sensing to the senescence
318 program, we next compared the phenotypic and transcriptional states of proliferating and p53-
319 restored senescent NSP tumor cells treated with recombinant IFN- γ at a low (50 pg/mL) or
320 higher (1 ng/mL) dose. While the addition of exogenous IFN- γ to proliferating or senescent
321 tumor cells had negligible effect on the viability, proliferation, or SASP gene expression of either
322 cell type at the doses tested (**Fig. 5A**; Supplementary Fig. S9A-S9D), marked changes in IFN- γ
323 pathway gene expression linked to the senescent state were observed. Specifically, supervised
324 clustering of the Hallmark “IFN- γ response signature” across proliferating and senescent cells
325 revealed three DEG modules: (i) genes that were downregulated during senescence
326 irrespective of IFN- γ (including the aforementioned negative regulators); (ii) genes that were
327 upregulated during senescence irrespective of IFN- γ and, interestingly, (iii) a substantial set of
328 DEGs that are cooperatively induced by the combination of senescence and IFN- γ (**Fig. 5B**).
329 Therefore, senescence triggers quantitative and qualitative changes in the transcriptional
330 response to IFN- γ .

331 One well-established output of IFN- γ signaling regulating cells’ susceptibility to adaptive
332 immune surveillance is an increased capacity for antigen presentation mediated by MHC class I
333 molecules (MHC-I) (47,52). Indeed, many of the genes upregulated in senescent cells (class ii
334 genes) or hyper-induced in the presence of exogenous IFN- γ (class iii genes) included

335 components of the antigen presentation machinery. Among the genes induced during
336 senescence (class ii genes) were *Tap1*, transporters associated with antigen processing, and
337 *Psmc1*, a proteasome factor associated with antigen processing (53). Those hypersensitive to
338 exogenous IFN- γ (class iii genes) included *Nlrc5*, a transcriptional co-activator of MHC-I genes
339 (54), the MHC-I assembly factor *Tapbp*, and the MHC-I subunit *B2m*. Two other class iii genes
340 were components of the immunoproteasome (*Psmc8*, *Psmc9*), whose actions can alter the
341 repertoire of presented peptides when overexpressed and are associated with an improved
342 tumor response to immune checkpoint blockade (55). This amplified output of IFN- γ in
343 senescent cells was confirmed by RT-qPCR and was retained at even higher levels of
344 exogenous IFN- γ (**Fig. 5C**, Supplementary Table S3). Consistent with the multifactorial process
345 described above, this effect was not observed in proliferating tumor cells, even those
346 overexpressing an IFNGR1 cDNA and/or treated with IFN- γ (Supplementary Fig. S10A-S10D).

347 Also consistent with the gene expression changes described above, senescent tumor
348 cells more robustly upregulate MHC-I in response to low levels of exogenous IFN- γ compared to
349 proliferating counterparts. Hence, while cell surface levels of MHC-I of both proliferating and
350 senescent cells were low at baseline and induced by exogenous IFN- γ , senescent cells showed
351 a significant increase of MHC-I protein expression (**Fig. 5D**). Similar synergies were observed
352 for cell surface HLA expression (identical to MHC-I in mice) in human cancer cells from liver and
353 other cancer types triggered to senescence with nutlin, which engages a p53-dependent
354 senescence program (56), or trametinib/palbociclib, which preferentially targets tumor cells with
355 an activated MAPK pathway [Supplementary Fig. S11A-S11D; ref. (20)]. Of note, the
356 combinatorial effects of drug treatment and IFN- γ on HLA expression required senescence
357 induction and did not occur in liver tumor cells that failed to senesce owing to a spontaneous or
358 engineered p53 mutation (irresponsive to nutlin) or a non-hyperactivated MAPK pathway
359 (irresponsive to trametinib/palbociclib). Furthermore, even though type I and type II IFN

360 response pathways include overlapping components, exogenous IFN- β treatment could not
361 substitute for IFN- γ in producing a robust MHC-I induction in senescent cells nor a strongly
362 differential induction between proliferating and senescent cells in our p53 restoration model
363 (Supplementary Fig. S11E and S11F). These data imply that murine and human cells triggered
364 to senesce acquire an increased capacity for antigen processing and presentation in the
365 presence of limiting quantities of IFN- γ .

366 **Senescent tumor cells hyperactivate the IFN- γ signaling pathway *in vivo***

367 To determine the *in vivo* consequences of the rewiring of IFN- γ signaling identified in
368 senescent cells, we next adapted an IFN- γ sensing (IGS) reporter system to directly visualize in
369 intracellular IFN- γ signaling activation in real time (57). This reporter consists of a series of
370 consensus interferon gamma-activated sequences, which has specificity to type II IFN over
371 other signals (57), followed by a cDNA sequence encoding ZsGreen1 fluorescent protein and is
372 linked to a constitutively expressed RFP transgene to visualize transduced cells (**Fig. 6A**). NSP
373 tumor cells expressing this construct were RFP positive and showed a dose-dependent
374 increase in ZsGreen1 signal upon treatment with IFN- γ *in vitro* that increased following p53
375 induction or following treatment with senescence-inducing drugs (**Fig. 6B**; Supplementary Fig.
376 S12A and S12B).

377 We next used this system to monitor signaling activity following senescence induction in
378 tumors. Reporter-transduced tumor cells (on Dox) expressing constitutive RFP were injected
379 into the livers of Dox-fed syngeneic recipients and, upon tumor manifestation, doxycycline was
380 removed to induce p53 expression and trigger senescence as above (see Figures 1 and 2).
381 Regressing tumors were isolated 9 days post Dox withdrawal for 3D imaging of reporter activity
382 and parallel assessment of IFN- γ signaling in comparison to proliferating controls (from mice
383 maintained on Dox). As illustrated in Fig. 6C, proliferating tumor cells showed little, if any,
384 reporter expression, whereas tumor cells triggered to senesce *in vivo* displayed a more

385 prominent ZsGreen1 signal (**Fig. 6C and 6D**; Supplementary video S2). This effect coincided
386 with a specific increase in levels of IFN- γ protein (but not Type I IFN) in tumor tissue extracts
387 (**Fig. 6E**; Supplementary Fig. S12C).

388 To test whether the altered composition of immune cells in senescent tumors (Fig. 2;
389 supplementary Fig. S5-S6) contributed to the enhanced signal of the IFN- γ sensing (IGS)
390 reporter, we performed *in vitro* co-culture assays allowing exposure of senescent or proliferating
391 tumor cells to equal number of activated CD8 T cells, which we identified via scRNA-seq data
392 as the predominant cellular source of IFN- γ *in vivo* (**Fig. 6F-6H**). Senescent cells still showed a
393 significant increase of ZsGreen1 signal as compared to proliferating controls (**Fig. 6I**).
394 Consistent with a non-cell-autonomous signaling activation, IFN- γ was not detected in
395 conditioned media from NSP tumor cells under proliferative or senescent conditions
396 (Supplementary Fig. S12D), yet IFN- γ was readily detected upon co-culture with CD8 T cells, an
397 effect that was further enhanced by the addition of macrophages and associated with increased
398 MHC class I on senescent cells as well as increased activation of CD8+ T cells (Supplementary
399 Fig. S12E-S12J). Collectively, these data support a model whereby heterotypic interactions
400 between senescent tumor cells and immune cells sensitizes the tumor to exogenous IFN- γ ,
401 leading to enhanced antigen presentation and efficient immune surveillance.

402 **IFN- γ signaling in senescent tumor cells is necessary for immune surveillance**

403 Our results imply that the immune-mediated clearance of senescent NSP tumor cells
404 involves the combined effects of SASP, known to stimulate immune cell recruitment (10,20,58),
405 together with a previously underappreciated capacity of senescent cells for enhanced sensing
406 and response to extracellular signals, as shown here with IFN- γ . To test the contribution of the
407 senescence-associated IFN- γ sensing program to the immune surveillance of senescent tumor
408 cells, we examined how disruption of the IFNGR in the tumor cells, or IFN- γ depletion in the
409 host, impacts the clearance of NSP tumor cells upon senescence induction. Indeed, tumor

410 regression (but not senescence *per se*) (Supplementary Fig. S13A-S13D) was impaired upon
411 knock-out (KO) of IFNGR1 (**Fig. 7A and 7B**; Supplementary Fig. S14A-S14C), an effect that
412 was even more pronounced for IFNGR-intact tumors engrafted into *Ifng*^{-/-} mice (**Fig. 7C and 7D**)
413 and associated with the expected loss of surface MHC-I in tumor cells (Supplementary Fig.
414 S14D and S14E).

415 Consistent with the known contribution of IFN- γ signaling and tumor cell MHC-I to CD8+
416 engagement (59), tumors that lacked IFNGR1 or that developed in *Ifng*^{-/-} recipients contained
417 fewer CD8+ T cells than their WT counterparts in both proliferating and senescent states
418 (Supplementary Fig. S14F), while still inducing robust immune infiltrate including abundant
419 macrophages (**Fig. 7E and 7F**; Supplementary Fig. S14G). Regardless, the impaired
420 senescence surveillance phenotype was not simply a result of this decrease in CD8+ T cells.
421 Co-culture assays providing uniform exposure of IFNGR1-KO and WT tumor cells to CD8 T
422 cells and macrophages still showed IFNGR1-dependent killing of senescent tumor cells
423 (Supplementary Fig. S15A-S15E)—a dependence that required the presence of both T cells
424 and macrophages and that not was observed in proliferating tumor cells under the same
425 conditions. Taken together, these data indicate that enhanced ability of senescent cells to sense
426 microenvironmental IFN- γ acts in concert with SASP-stimulated immune cell recruitment to
427 enable mutually reinforcing heterotypic interactions among tumor cells, macrophages, and
428 activated T cells that improve antigen presentation and immune surveillance, leading to potent
429 tumor regressions.

430

431 **DISCUSSION**

432 Enabled by a murine tumor model in which cancer immune evasion versus senescence
433 surveillance is under tight genetic control, we reveal how senescent cells dramatically alter their
434 ability to both send and receive environmental signals (Supplementary Fig. S16). Consistent
435 with known senescence programs, p53-driven senescence induction led to the silencing of
436 proliferative genes and induced the SASP. However, we also observed a profound effect on
437 gene expression for plasma membrane proteins, including a range of growth factor receptors
438 and cytokine receptors that are predicted to drastically alter how senescent cells respond to
439 environmental signals. Importantly, while we employed a liver cancer model as our primary
440 experimental system, a similar rewiring in the expression of cell surface sensors and gene
441 programs sensitizing to environmental signals was observed in a broad range of murine and
442 human tumor cells treated with senescence inducing agents, implying that the altered sensing
443 program is a general hallmark of the senescent state.

444 One of the prominent sensing pathways altered in senescent cells involves type II IFN
445 signaling. In our liver cancer model and across all senescent states we examined, senescence
446 is accompanied by cell-intrinsic transcriptional and protein expression changes predicted to
447 enhance signaling from exogenous IFN- γ . Indeed, senescent cells more robustly activated IFN-
448 γ effectors in response to IFN- γ *in vitro* and *in vivo*, and both an intact IFN- γ effector pathway
449 and IFN- γ in the environment are required for efficient CD8 T cell-mediated clearance of
450 senescent tumor cells. While pathway analysis of senescent cell transcriptomes invariably
451 identifies type II IFN signaling as an enriched feature, overlaps between type I and type II
452 signaling components and the fact that IFN- γ is typically not detected as a SASP factor have left
453 mechanistic questions regarding type II IFN signaling in senescence largely unexplored. Our
454 studies demonstrate that such enrichment in IFN signaling signatures of senescent cells reflects
455 an enhanced capacity for IFN- γ sensing whose output is most prominent *in vivo*.

456 Perhaps the most well-established output of type II IFN signaling involves its ability to
457 induce the antigen presentation machinery. Indeed, IFN- γ induced cell surface expression of
458 MHC-I (or HLA in human cells) in our model under both proliferating and senescence conditions.
459 However, IFN- γ -induced MHC-I upregulation was more pronounced in senescent cells, an effect
460 that correlated with increased expression of the transporter associated with antigen processing,
461 other antigen processing factors, and structural components of MHC-I. A similar hypersensitivity
462 to IFN- γ in inducing MHC-I/HLA was observed in human liver and lung cancer cell lines
463 triggered to senesce. These results imply that the senescence program can enhance antigen
464 presentation in non-immune cells, thereby facilitating tumor immunosurveillance.

465 Our results support a model whereby the ultimate impact of senescent cells on tissue
466 biology is dictated by the combined effects of how they send and receive environmental signals.
467 Not only do senescent cells induce the SASP, which triggers tissue remodeling and alters the
468 cell state and composition of immune cells in the environment, but they also dramatically alter
469 their surfaceome, leading to a differential ability to sense environmental factors, herein
470 exemplified by IFN- γ . Importantly, disruption of IFN- γ signaling had no effect on senescence
471 induction or the SASP in our system yet impaired subsequent tumor regressions, indicating that
472 altered environmental sensing acts in concert with the SASP to determine the ultimate output of
473 the senescence program – in this case, immune surveillance. These effects appear to be part of
474 a coordinated epigenetic program, as both the SASP and sensing programs show a prominent
475 dependence on the chromatin remodeling factor BRD4.

476 While the mechanism of immune surveillance in our model depends on cooperative
477 effects of CD8⁺ T cell and macrophage populations reflective of a transition from an “immune
478 cold” to an “immune hot” tumor microenvironment, other innate or adaptive immune cell types
479 may recognize and clear senescent cells in different contexts or, alternatively, immune
480 surveillance may not occur at all (18,19). Undoubtedly, some of these distinctions reflect
481 heterogeneity in SASP factor secretion (13,14), though our results raise the possibility that the
482 extent and nature of altered environmental sensing may also influence how senescent cells

483 affect tissue biology. While knockout of IFN- γ sensing (via *Ifngr1* knockout) and deletion of
484 MHC-I (B2M-KO) in senescent tumor cells impaired their immune surveillance *in vivo*, it did not
485 completely abolish tumor regression after senescence induction, indicating that IFN- γ sensing in
486 senescent cells is not the only pathway contributing to tumor regression. Regardless, the fact
487 that senescent cells can respond differently to environmental signals implies that their ultimate
488 molecular state in tissues will be different than in cell culture, highlighting the need to better
489 characterize the process *in vivo*.

490 Our results may help explain the paradoxical effects of senescence biology in physiology
491 and disease and have implications for the effective use of senescence-modulating therapeutics.
492 For example, in our model, the difference between tumor senescent cell clearance and
493 persistence was determined, at least in part, by the presence of environmental IFN- γ and the
494 integrity of the type II IFN signaling in the senescent cells. This suggests that variation in the
495 ability of senescent cells to recruit and sense IFN- γ secreting immune cells or other immune cell
496 types could profoundly affect senescent cell clearance, such that decreased environmental IFN-
497 γ or diminished type II IFN signaling could enable senescent cell persistence within tissues. In
498 the context of cancer, therapies that induce tumor cell senescence –a cytostatic program– can
499 trigger immune-mediated tumor regression or re-sensitize tumors to immune checkpoint
500 blockade, yet these are not the universal outcomes. As such, heterogeneity in the SASP (which
501 can vary between tumor cell types and senescence inducers) or IFN- γ sensing and output
502 (perhaps affected by deletion or mutation of IFN- γ pathway or HLA components (60) or the
503 reversible transcriptional mechanisms uncovered here) may influence the effectiveness of such
504 therapies in patients. Consistent with this notion, therapy-driven induction of specific SASP
505 profiles predicts patient outcomes in a subgroup of ovarian cancer patients (61). By contrast,
506 strategies to enhance the immune surveillance of senescent cells by increasing their sensitivity
507 to IFN- γ (e.g. with PTPN2 inhibitors) may help bias program output towards tumor cell rejection.
508 We envision that investigating this and other tissue remodeling and sensing programs in pre-
509 and post-treatment tumor biopsies (e.g. through transcriptomic or proteomic profiles) may

510 expose new response biomarkers and/or combination strategies to improve the clinical
511 management of cancer.

512 MATERIALS AND METHODS

513 Cell culture and drug treatment

514 p53-restorable mouse liver cancer cell lines were cultured in DMEM supplemented with 10%
515 FBS and 1% penicillin and streptomycin (GIBCO) on plates that were collagen-coated (PurCol,
516 Advanced Biomatrix, 0.1 mg/ml) for 30' at 37 C and maintained by the addition of 1 µg/ml
517 doxycycline to suppress p53 expression. In order to restore p53 expression and therefore
518 induce senescence, doxycycline-containing media was replaced with doxycycline-free media for
519 6 to 8 days. Cells were replated every 2 to 3 days to wash off doxycycline. Several cell lines
520 have been generated and NSP is predominantly used for the study given the robustness of
521 senescence phenotype upon p53 restoration. For human liver cell lines, HepG2 and SK-Hep1
522 were cultured with EMEM and SNU447 was cultured in RPMI-1640 in non-coated, tissue culture
523 treated plates, all supplemented with 10% FBS and 1% penicillin and streptomycin. For human
524 lung cancer cell lines, A549, H460 and H2030 were cultured in DMEM in non-coated, tissue
525 culture treated plates supplemented with 10% FBS and 1% penicillin and streptomycin. All
526 human cell lines were obtained from ATCC. Both murine and human cell lines were tested with
527 Mycoplasma regularly every 6 months. The concentration and regimen of drug treatment in
528 cancer cell lines were as followed. For perturbing BRD4-dependent transcriptional programs,
529 cells were treated with 500 nM of JQ-1 (S7110, Selleck Chem) for 48 h prior to harvest, starting
530 JQ-1 at day 6 after restoring p53 (off-Dox), when NSP cells are fully senescent. For drug-
531 induced senescence experiments, p53-suppressed (on-Dox) NSP cells were treated with
532 trametinib (25 nM, S2673 Selleck Chem) + Palbociclib (500 nM, S1116, Selleck Chem), Nutlin
533 (10 µM, S1061, Selleck Chem) or Cisplatin (1 µM), changed every 2-3 days, during 7 days. The
534 concentration of DMSO corresponded to the drug treatment and does not exceed 1:1,000
535 dilution of total media volume, which shows no discernable toxicity to cultured cells. For IFN-γ of
536 proliferating or senescent populations, the indicated doses of mouse or human recombinant
537 IFN-γ were administrated to murine and human cancer cell lines respectively after 24 h of cell

538 seeding and cells were harvested after 24 h of IFN- γ treatment for phenotypic or molecular
539 analyses.

540

541 **Cell culture and drug treatment**

542 Primary liver tumor generation and isolation of liver cell lines

543 All mouse experiments were approved by the Memorial Sloan Kettering Cancer Center (MSKCC;
544 New York, NY) Internal Animal Care and Use Committee. Mice were maintained under specific
545 pathogen-free conditions, and food and water were provided ad libitum. C57BL/6N female mice
546 aged 8-9 weeks old were injected via hydrodynamic tail vein injection (HTVI) with a sterile 2 ml
547 (or 1/10 of mouse body weight) 0.9% NaCl solution containing 5 μ g of pT3-EF1a-NrasG12D-
548 IRES-rtTA (Tet-On system) and 20 μ g of pT3-TRE-tRFP-shp53 transposon vectors along with 5
549 μ g CMV-SB13 transposase (5:1 ratio) through the lateral tail vein. Doxycycline was
550 administered to mice via 625 mg/kg doxycycline-containing food pellets (Harlan Teklad) at least
551 4 days before injection. The tumor was harvested at 5-7 weeks after injection for cell line
552 isolation. To derive cancer cell lines from primary liver tumor, tumors were minced and digested
553 with 5ml of digesting solution, containing 1 mg/ml collagenase IV (C5138, Sigma-Aldrich) and
554 0.3% Dispase II (Roche 04942078001) in DMEM, at 37 °C for 30 mins with occasional vortexing.
555 The cells were spun down to remove the supernatant and plated on collagen-coated plate.
556 Independent cell lines were passaged at least 7-8 passages to remove fibroblasts and obtain
557 homogenous population. For those experiments involving bioluminescence tracking of tumor
558 growth the transposon construct pT3-EF1a-NrasG12D-IRES-rtTA-IRES-Luc was used. In the
559 Tet-OFF system setting, the transposon construct pT3-EF1a-NrasG12D-IRES-tTA was used to
560 co-inject with pT3-TRE-tRFP-shp53 vector into mice under normal diet to allow p53 hairpin
561 expression. To restore p53 in the liver tumor, the mice were subjected to doxycycline diet. For
562 constitutive p53 knockdown model, transposon constructs pT3-EF1a-NrasG12D and pT3-EF1a-
563 tRFP-shp53 were used.

564

565 Orthotopic transplant experiments

566 Both C57BL/6 mice were predominantly used for the animal study for the HTVI tumor
567 generation and orthotopic liver injection experiments in the immunocompetent setting.
568 C57BL/6N strain was mainly used except for the matching control strain with IFNG KO mice
569 (Jax, #002287) that was in the C57BL/6J background. No difference was observed in terms of
570 tumor growth or senescence surveillance phenotype between C57BL/6N and J strain. Female
571 mice were used in the experiment for the convenience of cage separation. All *in vivo*
572 experiments were performed with age-matched (8-13 weeks old) cohorts. For the orthotopic
573 liver tumor injection, NSP tumor cells were trypsinized and filtered twice using 40 µm strainer to
574 reduce cell doublets followed by pelleting and were prepared in 20 µl of 1:1 DMEM to Matrigel
575 ratio and injected using 31-gauge needle to the left lobe of the mouse liver following the
576 standard microsurgery institutional practice. Due to the engraftment differences in mice of
577 different strains- C57BL/6, Nude and R2G2 (Envigo) mice- different amounts of tumor cells were
578 injected. Specifically, 5×10^5 , 8×10^4 and 5×10^4 cells were injected respectively in each strain to
579 have comparable tumor size around 2 weeks after injection. Mice were then randomized based
580 on the similar size of tumor and assigned to different groups for the subsequent experimental
581 design.

582

583 **Lentiviral and retroviral production and transduction**

584 Lentiviruses were generated by co-transfection of viral vectors (1.5 µg) with packaging plasmids
585 psPAX2 (0.75 µg) and pCMV-VSVG (0.25 µg) (Addgene) into 293T cells with 90% confluency in
586 a 6-well plate. Retroviruses were generated by co-transfection of viral vectors (2 µg) with pCMV-
587 VSVG (0.25 µg) (Addgene) into Phoenix-gp cells with 90% confluency in a 6-well plate.
588 Polyethyleneimine (PEI) was added during co-transfection with a ratio of total DNA:PEI = 1:3 to

589 facilitate the binding of the plasmid to the cell surface. Viral containing supernatants were
590 cleared of cellular debris by 0.45 µm filtration. Target cells were exposed to viral supernatants
591 and mixed with 4 µg/ml polybrene for overnight before being washed, grown for 24 h in fresh
592 media, then subjected to antibiotic selection or fluorescence-based cell sorting.

593

594 **Lentiviral and retroviral vectors**

595 Murine liver cancer cells were infected with retroviral vector MSCV-Luc2-IRES-GFP (62) to
596 enable bioluminescence imaging. For visualization and staining of liver tumor cells *in vivo*, tumor
597 cells were infected with either the following lentiviral vectors specified in the figure legends,
598 pRRL-SFFV-GFP-mirE(shRen)-PGK-puromycin (SGEP was a gift from Johannes Zuber,
599 Addgene #111170) or pRRL-EFS-GFP-shRen (generated through replacing SFFV with EFS
600 promoter and removing antibiotic selection marker puromycin), to label the cells with GFP. For
601 visualization of IFN-γ sensing, tumor cells were infected with the lentiviral IGS reporter construct
602 described below.

603

604 **Genetic manipulation of cell line using CRISPR/Cas9**

605 In order to knock out specific genes in mouse and human liver tumor cell lines, the plasmid
606 pSpCas9(BB)-2A-GFP (PX458) (PX458 was a gift from Feng Zhang, Addgene #48138) in which
607 a sgRNA targeting either an intergenic region of chromosome 8 (Ctrl) or the specific gene of
608 interest was cloned. Cells were transiently transfected by PEI (2 µg plasmid and 6 µl PEI in 6
609 well plate with 60% confluency). Transfected cells were subsequently FACS sorted by GFP
610 positivity 36-48 h post-transfection. For *Ifngr1* and *B2m* KO experiment, PX458 transfected cells
611 were first stained with IFNGR1 (2E2, biotin) followed by Streptavidin-APC staining, and MHC-I
612 (H-2K^b; AF6-88.5.5.3) antibody respectively and negative cells were sorted. Sorted population
613 were further tested with IFN-γ to evaluate KO efficiency by using MHC-I induction as a proxy. In
614 order to generate p53 KO human tumor cells, cells were electroporated following manufacturer's

615 instructions. Briefly, cells were trypsinized, washed in PBS once, and counted and then
616 resuspended in Neon Buffer R. In parallel, 1 µg of Cas9 (ThermoFisher) and 1 µg of sgRNA
617 were complexed for 15 min at room temperature to form the Cas9 RNP complex, which was
618 then mixed with the cell aliquot. The cell/RNP mixture was electroporated (1400 V pulse voltage,
619 20 ms pulse width, 2 pulses) using Neon electroporation system (Thermo Fisher). The cells
620 were recovered for 3 days with further selection through nutlin treatment (10 µM, Selleck
621 Chemicals S1061) for 5-7 days to enrich p53 KO cells. The sgRNA sequence used in the
622 experiments are: *lfng1*: TGGAGCTTTGACGAGCACTG, *B2m*: AGTATACTCACGCCACCCAC,
623 *Ctrl*: GACATTTCTTTCCCCACTGG and *TP53*: CGCTATCTGAGCAGCGCTCA.

624

625 **Co-culture assays**

626 In order to isolate CD8⁺ T cells from spleens of female OT-I mice (Jackson laboratory), spleens
627 were mechanically disrupted by passing them through a 70 µm cell strainer and centrifuged at
628 1500 rpm x 5 minutes. Red blood cells were lysed with ACK lysis buffer (Quality Biological) for 5
629 minutes. Total splenocytes or CD8⁺ T cells FACS sorted on a Sony MA900 were then activated
630 with CD3/CD28 Dynabeads (one bead/T cell, Thermo Fisher) and cultured in presence of IL-2
631 (2 ng/ml; Biolegend), IL-7 (2.5 ng/ml; Peprotech), IL-15 (50 ng/ml; Peprotech) and 2-
632 mercaptoethanol (5.5µM, Fisher Scientific) in complete RPMI-1640 media supplemented with
633 10% FBS and 100 IU/ml penicillin/streptomycin for 5-6 days (passage cells every 2-3 days) prior
634 to co-culture assays with mouse liver tumor cells. For Kupffer cells isolation, BL/6 male mice
635 aged 8-14 weeks were first subjected to liver perfusion as previously described (63). After
636 perfusion, the liver was removed and homogenized and then digested with protease solution
637 (0.5 mg/ml type XIV protease, Sigma, P5147) supplemented with DNase I (0.2 µg/ml, Roche,
638 10104159001) for 15 minutes at 37C with constant stirring. This suspension was then
639 centrifuged at 50 g for 3 minutes to remove the hepatocyte pellet. The supernatant was then
640 transferred and centrifuged 580 g for 5 minutes at 4C. Next, the pellet was washed with HBSS

641 to remove residual protease solution and centrifuged at 580 g for 5 minutes at 4C to pellet the
642 cells again. The pellet was then resuspended with FACS buffer and subjected to α -F4/80
643 isolation according to the manufacturer instruction (Miltenyi Biotec, 130-110-443). After isolation,
644 the purity of Kupffer cells was confirmed with F4/80 staining through flow cytometry.

645 Murine liver tumor cells NSP were transduced with retrovirus expressing PresentER-SIINFEKL
646 construct (GFP) (PresentER-SIINFEKL (GFP) was a gift from David Scheinberg, Addgene
647 #102944) to express the peptide 257-264 from chicken ovalbumin, which is presented by H-2Kb
648 on the cell surface. Transduced cells were further selected with puromycin to obtain > 95% GFP
649 positivity. Tumor cells were cultured in presence or absence of doxycycline for 6 days in order to
650 induce senescence. 1,000 proliferating or 2,000 senescent tumor cells were plated in the
651 individual well of a 96 well collagen-coated plate. For those experiments where Kupffer cells
652 were added, they were isolated on the same day and plated at the indicated ratio 6 h after
653 plating the tumor cells. 24 h after plating tumor cells, previously activated OT-I T cells were
654 added at the indicated ratio. Co-cultures were imaged over time using an INCell 6000 high-
655 content imager (GE Healthcare Life Sciences), with a 488 nm and a 633 nm laser excitation to
656 visualize tumor cells and T cells (stained by CellTracker Deep Red Dye, Invitrogen C34565)
657 respectively, using a 10x objective. Images were captured at indicated time points, starting after
658 the seeding of T cells onto tumor cells/Kupffer cells co-cultures. Images for each channel were
659 saved during the experiment and subsequently analyzed using Columbus image analysis
660 software. GFP+ tumor cells were identified and segmented from background using an intensity-
661 based threshold method. T cells were identified using the same threshold method as the tumor
662 cells. Number of the GFP+ tumor cells was quantified and normalized to the untreated control to
663 calculate the killing index.

664

665 *IFNGR1 KO and WT tumor cell mixture in co-culture experiment*

666 For IFNGR1 WT vs. KO mixture experiment (supplementary figure S15E), cells were mixed and
667 kept on or off Dox for 6 days before starting the co-culture experiment using a 24-well plate by
668 plating 7,000 and 14,000 proliferating and senescent cells respectively with the same protocol
669 described above. The percentage of IFNGR1 WT vs. KO cells and absolute number (through
670 counting beads) were measured by flow cytometry.

671

672 *Effect of cell-cell contact between macrophages and CD8 T cells in co-culture experiment*

673 To measure the effect of direct contact of macrophages with CD8 T cells, we used a transwell
674 plate (Costar 12mm transwell, 0.4 μm pore, #3460) to separate macrophage and CD8 T+tumor
675 cells by plating macrophages at the bottom well while the CD8 T cells and tumor cells were
676 plated on the upper well. As a comparison, 24-well plate with 3 cell types co-cultured together
677 were used. After 48 h, T cells were collected and stained for antibodies and subjected to flow
678 cytometry.

679

680 **Proliferation and SA- β -gal assays**

681 For colony formation assays, 2,500 mouse liver cancer cells or 10,000 human liver cancer cells
682 were plated in each well of a 6-well plate. Cells were cultured for 6 days, then fixed with 4%
683 formaldehyde, and stained with crystal violet. Detection of SA- β -gal activity was performed as
684 previously described at pH 5.5 for mouse cells and tissue and pH 6 for human cells (20). For *in*
685 *vivo* SA- β -gal staining, fresh frozen tissue sections were fixed with 0.5% glutaraldehyde
686 followed by standard SA- β -gal staining as above described. Sections were counterstained with
687 eosin. For population doubling curves, cells were washed with PBS, trypsinized, and 100,000
688 cells were plated in triplicates in 6-well plates in presence or absence of doxycycline. Every 48 h
689 cells were counted and 1×10^5 cells were replated. Population doublings for each 48 h period
690 were calculated by dividing the final cell number to initial cell number.

691

692 **Whole mount immunostaining and tissue clearing**

693 To detect T cells and neutrophils in the NSP liver tumors, we performed whole mount
694 immunostaining and tissue clearing (with benzyl alcohol, benzyl benzoate, BABB) of excised
695 tumors as previously described (32). At the indicated time points, mice were euthanized by
696 carbon dioxide inhalation and liver tumors collected and fixed in 4% paraformaldehyde in PBS
697 at 4°C overnight. Tissues were washed three times with PBS for 10' at room temperature and
698 preserved in 0.05% azide in PBS at 4 °C before processing. Then, the tissues were
699 permeabilized in methanol (MetOH) gradients in PBS (PBS > 50% MetOH > 80% MetOH >
700 100%MetOH, 30 min in each solution), bleached with Dent's bleach (15% H₂O₂, 16.7% dimethyl
701 sulfoxide [DMSO] in MetOH) for 1h at room temperature, and rehydrated through descending
702 MetOH gradients in PBS (80% MetOH > 50% MetOH > PBS, 30 min in each solution). Tissues
703 were next incubated in blocking buffer (0.3% Triton X100, 0.2% BSA, 5% DMSO, 0.1% azide
704 and 25% FBS in PBS) for 24h at 4°C on a shaker and then stained with antibodies (rat anti-CD3
705 [clone 17A2, cat#100202, Biolegend, RRID:AB_312659]; goat anti-myeloperoxidase [goatMPO,
706 AF3667, R&D Systems, AB_2250866], and [hamster anti-CD31, 2H8, MA3105, Thermo Fisher,
707 RRID:AB_223592] all diluted 1:200 in blocking buffer), for 3 days at 4°C on a shaker. Tissues
708 were next washed for 24 h in washing buffer (PBS with 0.2% Triton X100 and 3% NaCl), and
709 stained with secondary antibodies (donkey anti-rat-AF488 [A212008, Invitrogen] and donkey
710 anti-goat AF647 [A21447, Invitrogen] diluted at 1:400 in blocking buffer) for 2 days at 4°C with
711 shaking. Tissues were then washed for 24 h in washing buffer and thereafter stained with goat
712 anti-hamster-AF568 (goat anti-hamster IgG (H+L) cross-adsorbed secondary antibody, Alexa
713 Fluor 568, A21112, Thermo Fisher, diluted at 1:400) and (1:1000) in blocking buffer for 2 days
714 at 4°C, on a shaker. Tissues were then washed for 24 h in washing buffer and thereafter
715 dehydrated in MetOH gradients in dH₂O using glass containers (50% MetOH > 70% MetOH >
716 90% MetOH > 3x 100% MetOH, 30 min for each step). Tissues were next cleared for 30 min in
717 50% MetOH and 50% BABB (benzyl alcohol, benzyl benzoate, mixed 1:2) followed by clearing 1

718 h in 100% BABB. Finally, the tissues were imaged on an SP8 Microscope (Leica). Visualization
719 and quantification was performed with Imaris software (Bitplane). In separate experiments, 3D
720 imaging after tissue clearing was used to detect the ZsGreen1, IFN- γ sensing (IGS) reporter.
721 For these experiments, we used the CUBIC tissue clearing protocol that maintains the
722 fluorescence from fluorescent proteins (64). Tissues were excised and fixed as stated above,
723 and then were soaked in CUBIC-I solution in a 15 mL conical tube container. CUBIC-I was
724 prepared mixing 108 ml of ddH₂O with 75g of Urea (Sigma, U5128), 75g of N,N,N',N'-Tetrakis(2-
725 Hydroxypropyl)ethylenediamine (Sigma, 122262) and 42ml of Triton X-100 (Sigma, X100).
726 Samples were maintained at 37°C on a shaker for 7 days, changing the media every other day,
727 until clear. The samples were then counterstained for DAPI in CUBIC-1 (1:1000) for 24h and
728 washed in CUBIC-I overnight. Images were acquired and analyzed as described above.

729

730 **Western blotting**

731 Cells were lysed with RIPA buffer (50 mM Tris PH 7.4, 150 mM NaCl, 0.5 % sodium deoxycholate,
732 0.1% SDS; 1mM EDTA; 1% NP-40) supplemented with phosphatase and protease inhibitor
733 (5872, Cell Signaling Technology) and protein concentration was determined by BCA assay.
734 Samples were boiled for 5 minutes and 20 to 30 μ g of protein were separated by SDS-PAGE,
735 transferred to polyvinylidene difluoride (PVDF) membranes (Millipore) according to standard
736 protocols and probed with the relevant primary antibody overnight at 4°C. Membranes were
737 then incubated with horseradish peroxidase (HRP)-conjugated anti-rabbit IgG or anti-mouse IgG
738 secondary antibodies (1:10,000, GE Healthcare Life Science) at room temperature and proteins
739 were detected using Pierce ECL Western Blotting Substrate (34095, Thermo Fisher Scientific).
740 Antibodies were diluted as follows: p53 (CM5) (1:500, NCL-L-p53-CM5p, Leica Biosystems,
741 RRID:AB_2895247), p21 (F-5) (1:500, sc-6246, Santa Cruz Biotechnology, RRID:AB_628073),
742 phospho-STAT1 (Tyr701) (1:500, #9167, Cell Signaling Technology, RRID:AB_561284),
743 STAT1 (1:1,000, #14994, Cell Signaling Technology, RRID:AB_2737027), JAK1 (1:1000, #3344,

744 Cell Signaling Technology, RRID:AB_2265054), phosphor-JAK1 (1:1000, #3331, Cell Signaling
745 Technology, RRID:AB_2265057), TC-PTP (PTPN2, 1:1000, ab180764, Abcam,
746 RRID:AB_2722704). Protein loading was measured using a monoclonal β -ACTIN antibody
747 directly conjugated to horseradish peroxidase (1:20,000; A1978, Sigma-Aldrich,
748 RRID:AB_476692), NUCLEOLIN (1:5000, ab22758, Abcam, RRID:AB_776878) or VINCULIN
749 (1:2,000, ab129002, Abcam, RRID:AB_11144129). ECL developed blots were imaged using a
750 FluorChem M system (Protein Simple).

751

752 ***In vitro* multiplexed ELISA**

753 Conditioned media samples (duplicates collected in complete DMEM 48 h after seeding) from
754 proliferating or senescent NSP tumor cells (6 to 8 days after doxycycline withdrawal) were
755 centrifuged at 1500 rpm for 3 minutes and filtered through 0.2 μ m filter to remove cell debris.
756 Samples concentrations were normalized by diluting in complete DMEM according to cell count.
757 Aliquots (50 μ l) of the conditioned media were analyzed using multiplex immunoassays
758 designed for mouse (Mouse Cytokine/Chemokine Array 31-Plex) from Eve Technologies.
759 Biological replicates from two independent experiments were performed to determine cytokine
760 levels. Heatmaps display relative cytokine expression values normalized to geometric means of
761 individual cytokines from both proliferating and senescent samples.

762 **Measurement of IFN- γ in *in vivo* tumor lysates and *in vitro* conditioned medium**

763 BD cytometric bead array Mouse Th1/Th2 cytokine kit (Cat# 551287, BD Biosciences) was used
764 to determine the IFN- γ levels. Flash frozen tissues were lysed in RIPA buffer and homogenized
765 using TissueLyser II (Qiagen) followed by protein concentration measurement determined by
766 BCA assay. 100 μ g of tissue lysate were used for subsequent measurement following standard
767 manufacturer instructions of CBA kits. For *in vitro* conditioned medium measurement, 50 out of
768 200 μ l of conditioned medium collected from the 96 well of co-culture experiments were used.

769

770 **Plasma membrane-enriched mass spectrometry**

771 To capture differential cell surface proteome changes induced by senescence, we adapted the
772 protocol from previous published study (45) and followed the manufacturer instruction (Pierce
773 Cell Surface Protein Isolation Kit #89881) to enrich cell surface proteins of proliferating and
774 senescent cells through biotin-based labeling followed by pull-down purification. In brief, we
775 plated 1 and 3 15 cm plates of proliferating and senescent cells (6 days after doxycycline
776 withdrawal) with an initial seeding of 7×10^5 and 2×10^6 million cells respectively and collected the
777 cells 2 days later, with the cells approximately at 85% confluency. Before harvesting the cells,
778 cells were incubated with biotin solution for 30 minutes at 4C to allow the surface protein
779 labeling. Cells were then washed with cold PBS and scraped down followed by lysis (buffer
780 provided in the kit). Lysates were centrifuged and the clarified supernatant was used for
781 purification of biotinylated proteins on NeutrAvidin Agarose. Supernatant was incubated with
782 NeutrAvidin Agarose for 2 h at room temperature in the closed column to allow biotinylated
783 proteins binding. Column containing Agarose slurry was washed to remove unbound proteins.
784 The proteins were then digested in situ in the column overnight using 4 μ g of trypsin (Promega,
785 V5111) per column at 37C on a rotor. Digested proteins were further desalted by C18 Stagetip
786 and subjected to liquid chromatography–mass spectrometry (LC-MS/MS) followed by proteins
787 identification through Proteome Discover (Thermo Scientific) according to protocols previously
788 described (45). Non-biotinylated cell lysates were also included and served as background
789 controls.

790

791 **Protein identification**

792 The LC-MS/MS .raw files were processed using Mascot and searched for protein identification
793 against the SwissProt protein database for human/mouse (please adjust the species
794 accordingly). Carbamidomethylation of C was set as a fixed modification and the following
795 variable modifications allowed: oxidation (M), N-terminal protein acetylation, deamidation (N and

796 Q), and phosphorylation (S, T and Y). Search parameters specified an MS tolerance of 10 ppm,
797 an MS/MS tolerance at 0.080 Da and full trypsin digestion, allowing for up to two missed
798 cleavages. False discovery rate was restricted to 1% in both protein and peptide level.
799 Normalized protein intensities were obtained using Scaffold (4.8.4).

800

801 **RNA preparation and High throughput RNA-sequencing analysis**

802 For *in vitro* liver cell lines RNA preparation, total RNA was extracted using TRIzol (Thermo
803 Fisher Scientific) following the manufacturer's instructions. For *in vivo* bulk tumor RNA-seq,
804 proliferating tumor (p53 Off) was harvested 7-10 day after randomization point and senescent-
805 induced tumor (p53 On) was harvested 12 days after p53 restoration, allowing similar size of
806 tumor at harvest. To extract tissue RNA, freshly isolated tumor chunk was first stored in RNA-
807 later solution (AM7024, Thermo Scientific) to preserve RNA integrity until extraction and
808 RNeasy kit (74106, Qiagen) was used to purified tissue RNA following the manufacturer
809 instructions. Purified polyA mRNA was subsequently fragmented, and first and second strand
810 cDNA synthesis performed using standard Illumina mRNA TruSeq library preparation protocols.
811 Double stranded cDNA was subsequently processed for TruSeq dual-index Illumina library
812 generation. For sequencing, pooled multiplexed libraries were run on a HiSeq 2500 machine on
813 RAPID mode. Approximately 10 million 76bp single-end reads were retrieved per replicate
814 condition. Resulting RNA-Seq data was analyzed by removing adaptor sequences using
815 Trimmomatic (65), aligning sequencing data to GRCm38 – mm10 with STAR (66), and genome
816 wide transcript count was quantified using featureCounts (67) to generate raw count matrix.
817 Differential gene expression analysis was performed using DESeq2 package (68) between
818 experimental conditions, using 3 independent biological replicates (independent cultures of NSP
819 tumor cells) per condition, implemented in R (<http://cran.r-project.org/>). Differentially expressed
820 genes (DEGs) were determined by > 2-fold change in gene expression with adjusted P-value <
821 0.05. For heatmap visualization of DEGs, samples were z-score normalized and plotted using

822 'pheatmap' package in R. Functional enrichments of these differential expressed genes were
823 performed with enrichment analysis tool Enrichr (69). Gene expressions of RNA-Seq data were
824 clustered using hierarchical clustering based on one minus Pearson correlation test. Subtype
825 specific gene signatures were derived (22) and used as inputs for signature score calculation
826 using R package singscore (70).

827

828 **Public dataset transcriptomic analyses**

829 Signature of different human liver cancer subtype was obtained from previous study (22). In
830 brief, the top 200 over-expressed and under-expressed gene transcripts among each tumor
831 subtype were selected as their signature. To analyze the transcriptomic changes of genes
832 encoding plasma membrane and extracellular factors distinguishing senescent and proliferating
833 tumor cells, transcriptomic data of a series of human tumor cell lines triggered to senesce was
834 used according to the previously published study (44) and obtained from the website
835 <https://ccb.nki.nl/publications/cancer-senesce/>. The expression of selected genes was
836 compared between senescent and the corresponding proliferating cells among individual cell
837 lines and normalized to determine the fold change. Information about protein subcellular
838 localization was derived from the Compartments_knowledge_based database (71), with the
839 genes assigned to specific subcellular localization when the criteria score is ≥ 3 . The Cancer
840 Genome Atlas Liver Hepatocellular Carcinoma (TCGA-LIHC) data set, including p53 mutational
841 status, transcriptomic profiles, and patient survival, were downloaded using R package
842 TCGAbiolinks (72,73). Senescence signatures derived from our mouse models were used as
843 input for computing signature scores using ssgsea method in R package GSVA (74). These
844 signature scores were used to separate patients into high and low groups, and log rank test was
845 used to test the differences in survival between these two groups.

846

847 **Gene set enrichment analysis (GSEA)**

848 GSEA was performed using the GSEAPreranked tool for conducting gene set enrichment
 849 analysis of data derived from RNA-seq experiments (version 2.07) against signatures in the
 850 MSigDB database (<http://software.broadinstitute.org/gsea/msigdb>), signatures derived herein,
 851 and published expression signatures in organoid models and human samples. The metric
 852 scores were calculated using the sign of the fold change multiplied by the inverse of the p-value.

853

854 **Reverse transcription and quantitative PCR**

855 Total RNA was isolated from mouse liver tumor cell line using TRIzol (Thermo Fisher Scientific)
 856 following the manufacturer's instructions. cDNA was obtained from 500 ng RNA using the
 857 Transcriptor First Strand cDNA Synthesis Kit (04896866001, Roche) after treatment with DNase
 858 I (18068015, Thermo Fisher Scientific) following the manufacturer's instructions using random
 859 hexamer method. The following primer sets for mouse sequences were used: Tap1_F 5'-
 860 GGACTTGCCTTGTCCGAGAG-3', Tap1_R 5'-GCTGCCACATAACTGATAGCGA-3',
 861 Psmb8_F 5'-ATGGCGTTACTGGATCTGTGC-3', Psmb8_R 5'-
 862 CGCGGAGAACTGTAGTGTCC-3', Nlrc5_F 5'-CCTGCGTCCCAGTCATTC-3', Nlrc5_R 5'-
 863 CTGCTGGTCAGTGATGGAGA-3', Erap1_F 5'-TAATGGAGACTCATTCCCTTGG-3', Erap1_R
 864 5'-AAAGTCAGAGTGCTGAGGTTT G-3', H2-K1_F 5'-GCTGGTGAAGCAGAGAGACTCAG-3',
 865 H2-K1_R 5'-GGTGACTTTATCTTC AGGTCTGCT-3', H2-D1_F 5'-
 866 AGTGGTGCTGCAGAGCATTACAA-3', H2-D1_R 5'-GGTGAC TTCACCTTTAGATCTGGG-3',
 867 B2m_F 5'-TTCTGGTGCTTGTCTCACTGA-3', B2m_R 5'-CAG TATGTTTCGGCTTCCCATTTC-3',
 868 Cdkn1a_F 5'-CGGTGTCAGAGTCTAGGGGA-3', Cdkn1a_R ATC ACCAGGATTGGACATGG-3',
 869 Trp53_F 5'-CTAGCATTTCAGGCCCTCATC-3', Trp53_R 5'-TCCGACTGTGACTCCTCCAT-3',
 870 Csf3_F 5'-ATGGCTCAACTTTCTGCCCAG-3', Csf3_R 5'- CTGACAGTGACCAGGGGAAC-3',
 871 Socs3_F 5'-ATGGTCACCCACAGCAAGTTT-3', Socs3_R 5'-TCCAGTAGAATCCGCTCTCCT-3',
 872 Ptpn2_F 5'-ATGTCGGCAACCATCGAGC-3', Ptpn2_R 5'- TGTTTCGGTTTCTGTTTTCTGGA-3',
 873 Irf1_F 5'- ATGCCAATCACTCGAATGCG-3', Irf1_R 5'-TTGTATCGGCCTGTGTGAATG-3',

874 Ccl5_F 5'-CTGCTGCTTTGCCTACCTCT-3', Ccl5_R 5'- CGAGTGACAAACACGACTGC-3',
875 Il18-F 5'-CAGGCCTGACATCTTCTGCAA-3', Il18-R 5'- TCTGACATGGCAGCCATTGT-3',
876 Hprt_F 5'-TCAGTCAACGGGGGACATAAA-3', Hprt_R 5'-GGGGCTGTACTGCTTAACCAG-3',
877 Rplp0_F 5'-GCTCCAAGCAGATGCAGCA-3', Rplp0_R 5'-CCGGATGTGAGGCAGCAG-3',
878 Quantitative PCR with reverse transcription (qRT-PCR) was carried out in triplicate (10 cDNA
879 ng per reaction) using SYBR Green PCR Master Mix (Applied Biosystems) on the ViiA 7 Real-
880 Time PCR System (Life technologies). Hprt, Rplp0 (also known as 36b4) served as endogenous
881 normalization controls.

882

883 **Tumor measurement by ultrasound and bioluminescence imaging**

884 High-contrast ultrasound imaging was performed on a Vevo 2100 System with a MS250 13- to
885 24-MHz scanhead (VisualSonics) to stage and quantify liver tumor burden. Tumor volume was
886 analyzed using Vevo LAB software. Bioluminescence imaging was used to track luciferase
887 expression in orthotopically injected liver tumor cells expressing a Luc-GFP reporter as well as
888 primary HTVI tumor harboring luciferase construct (vector described above). Mice were injected
889 IP with luciferin (5 mg/mouse; Gold Technologies) and then imaged on a Xenogen IVIS
890 Spectrum imager (PerkinElmer) 10 minutes later. Quantification of luciferase signaling was
891 analyzed using Living Image software (Caliper Life Sciences).

892

893 **Flow cytometry and sample preparation**

894 For *in vivo* sample preparation, orthotopically injected liver tumors were isolated by removing
895 the adjacent normal tissue, and allocated for 10% formalin fixation, OCT frozen blocks, snap
896 frozen tissue, and flow cytometry analysis. To prepare single cell suspensions for flow cytometry
897 analysis, liver tumor was mechanically disrupted to a single cell suspension using a 150 µm
898 metal mesh and glass pestle in ice-cold 3% FBS/HBSS and passed through a 70 µm strainer.

899 The liver homogenate was spun down at 400 g for 5 minutes at 4°C, and the pellet was
900 resuspended in 15ml 3% FCS/HBSS, 500ul (500U) heparin, and 8ml Percoll (GE), mixed by
901 inversion, and spun at 500 g for 10 min at 4°C. After removal of supernatant, cells were
902 resuspended in PBS supplemented with 2% FBS. Samples were blocked with anti-CD16/32
903 (1:200, FC block, #553142) (BD Pharmigen) for 20 minutes and then incubated with the
904 following antibodies for 30 minutes on ice: CD3 (1:200, 17A2, #612803, RRID:AB_2870130),
905 CD19 (1:200, 1D3, #563235, RRID:AB_2738085), CD4 (1:800, RM4-5, #563151,
906 RRID:AB_2687549), Ly6G (1:200, 1A8, #563005, RRID:AB_2737946), CD44 (1:200, IM7,
907 #560568, RRID:AB_1727481), CD11b (1:800, M1/70, #563553, RRID:AB_2738276) (BD
908 Biosciences); MHC-I (1:100, H-2k^b; AF6-88.5.5.3, #17-5958-82, RRID:AB_1311280), CD119
909 (1:100, 2E2, #13-1191-82, RRID:AB_2572773), Armenian Hamster IgG isotype (1:100,
910 eBio299Arm, #13488881, RRID:AB_470094) (Thermo Fisher); CD45 (1:400, 30-F11M,
911 #103128, RRID:AB_493715), Gr-1 (1:200, RB6-8C5, #108406, RRID:AB_313371), F4/80
912 (1:100, BM8, #123116, RRID:AB_893481), CD8 (1:400, 53-6.7, #100721, RRID:AB_312760),
913 Ly6C (1:200, HK1.4, #128026, RRID:AB_10640120), CD11c (1:200, N418, #117335,
914 RRID:AB_11219204), CD69 (1:200, H1.2F3, #104522, RRID:AB_2260065), CD106 (1:100,
915 MVCAM.A, #105717, RRID:AB_1877142), CD62L (1:200, MEL-14, #104435,
916 RRID:AB_10900082), PD-1 (1:100, 29F.1A12, #135215, RRID:AB_10696422) (Biolegend);
917 IFNGR2 (1:100, REA381, #130-105-670, RRID:AB_2652258) (Miltenyi Biotec); Streptavidin
918 (1:200, #20-4317-U100), TIGIT (1:100, 1G9, #20-1421-U025, RRID:AB_2621591), NK1.1
919 (1:100, PK136, #65-5941-U100, RRID:AB_2621910) (Tonbo); human antibody HLA-A,B,C
920 (1:100, W6/32, #17-9983-42, RRID:AB_10733389) (Thermo Fisher). To distinguish live/dead
921 cells, DAPI and Ghost dye violet 510 (1:1000, #13-0870-T100) (Tonbo) were used depending
922 on whether the cells are fixed. For fixed cells, cells were stained in PBS prior to antibody
923 staining. Flow cytometry was performed on an LSRFortessa or Guava flow cytometer (Luminex
924 Corporation), and data were analyzed using FlowJo (TreeStar).

925 **Neutralizing antibody and liposomal clodronate studies**

926 To determine the specific immune cell dependency of senescence surveillance, depleting
927 antibodies or drugs were administrated to the mice one day after doxycycline withdrawal. For
928 NK cell depletion, mice were injected intraperitoneally (IP) with an α -NK1.1 antibody (250 μ g;
929 PK136, BioXcell) twice per week. For T cell depletion, mice were injected IP with either an α -
930 CD4 (200 μ g; GK1.5, BioXcell) or α -CD8 antibody (200 μ g; 2.43, BioXcell) twice per week.
931 Depletion of NK, CD4+, and CD8+ T cells was confirmed by flow cytometric analysis of liver
932 tumor tissue. For neutrophil/myeloid-derived suppressive cells depletion, mice were injected
933 intraperitoneally with an α -Gr-1 (200 μ g; RB6-8C5, BioXcell) twice per week. For control, isotype
934 control antibody (200 μ g; LTF-2, BioXcell) was IP twice per week. For macrophage depletion,
935 mice were injected intravenously (IV) with clodronate liposomes (50 mg/kg of mouse weight;
936 ClodronateLiposomes.com) twice per week. PBS was used as a control.

937

938 **Immunofluorescence and immunohistochemistry**

939 Tissues were fixed overnight in 10% neutral buffered formalin (Richard-Allan Scientific),
940 embedded in paraffin and cut into 5 μ m sections. Sections were deparaffinized and rehydrated
941 with a histoclear/alcohol series and subjected to antigen retrieval by boiling in citrate antigen
942 retrieval buffer (Vector). Slides were then blocked in PBS/0.1% Triton X-100 containing 1% BSA.
943 Primary antibodies were incubated overnight at 4°C in blocking buffer. The following primary
944 antibodies were used: GFP (ab13970, Abcam, 1:500, RRID:AB_300798), Ki67 (#550609, BD
945 Biosciences, 1:200, RRID:AB_393778), CD8 (#14-0808-82, eBioscience, 1:200,
946 RRID:AB_2572861), CD45 (#70257, Cell Signaling Technology, 1:100, RRID:AB_2799780),
947 F4/80 (#70076, Cell Signaling Technology, 1:200), p21 (#556431, BD Biosciences, 1:200,
948 RRID:AB_396415). For immunohistochemistry, Vector ImmPress HRP kits and ImmPact DAB
949 (Vector Laboratories) were used for secondary detection. For immunofluorescence, the

950 following secondary antibodies were used: goat anti-chicken AF488 (A11039, Invitrogen, 1:500,
951 RRID:AB_2534096), donkey anti-rabbit AF594 (A21207, Invitrogen, 1:500, RRID:AB_141637),
952 goat anti-rabbit AF594 (A11037, Invitrogen, 1:500, RRID:AB_2534095), donkey anti-rabbit
953 AF647 (A31573, Invitrogen, 1:500, RRID:AB_2536183). All secondary antibodies were diluted in
954 blocking buffer and incubated for 1 h at room temperature. Subsequently, slides were washed
955 and nuclei were counterstained with PBS containing DAPI (1 µg/ml), and mounted under cover
956 slips with ProLong Gold (Life Technologies). Images were acquired with a Zeiss AxioImager
957 microscope using Axiovision software.

958
959 Triple immunofluorescence staining of PD-L1, CD68 and GFP of 2-3 µm sections was
960 performed using a Leica Bond RX platform (Leica Biosystems) with ER2 buffer (AR9640, Leica
961 Biosystems) for epitope retrieval. The following primary antibodies were used: PD-L1 (D5V3B,
962 #64988, Cell Signaling Technology, 1:150, 30min, RRID:AB_2799672), CD68 (orb47985,
963 Biorbyt, 1:1000, 30 min), GFP (TP401, Amsbio, 1:1000, overnight, after Opal protocol,
964 RRID:AB_10890443). Antibodies were detected using Opal 4-Color Automation IHC Kit
965 (NEL8720001KT, Akoya) with Opal 520 Reagent for PD-L1, Opal 570 Reagent for CD68, and
966 BrightVision Poly-HRP-Anti Rabbit antibody (DPVR-110HRP, Immunologic). GFP was
967 visualized using Donkey anti-Rabbit IgG (H+L) Alexa Fluor™ 647 (A31573, Thermo Fisher,
968 1:500, 1h, RRID:AB_2536183). Nuclei were stained with DAPI (D9542, Sigma). Specificity of
969 staining was confirmed with polyclonal rabbit IgG (Abcam, ab37415, RRID:AB_2631996).
970 Fluorescence images were acquired with a NanoZoomer-2.0 HT C9600 digital scanner
971 (Hamamatsu) and visualized with QuPath software (75) using the same settings.

972
973 **Generation of IFN-γ sensing (IGS) reporter**

974 In order to generate the IFN-γ sensing reporter from our study, we have adapted the construct
975 design from the previously described paper (57). In brief, we have crafted a 5x Interferon

976 Gamma-activated sequence (GAS) inserted in front of a mini promoter (minimal TATA-box
977 promoter with low basal activity) followed by ZsGreen1 reporter. Right after the reporter
978 sequence, this lentiviral construct also contains RFP driven by the PGK promoter to have
979 constitutive RFP expression for cell visualization. The cells were transduced with virus and
980 sorted through flow cytometry with high RFP level for stable expression of the construct in the
981 cells.

982

983 **Single-cell RNA-seq (scRNAseq) analyses**

984 Data pre-processing and QC

985 All scRNAseq data were processed into count matrices using 10x Genomics CellRanger 6.0.0
986 with default parameters using reference mouse genome GRCm38/mm10 augmented with
987 BioLegend TotalSeqB hashtag oligonucleotide barcode sequences for demultiplexing cellular
988 compartments in downstream analysis. Count matrices were processed to remove empty and
989 low quality droplets by removing (in order): transcripts with more than 10 million or fewer than
990 100 total reads, droplets with library size greater than 150,000 or lower than 300 total read
991 count, and droplets with fewer than 15 distinct expressed transcripts.

992

993 Potential doublets were removed using Solo version 1.2 (76) by training one doublet
994 classification model per sample using default parameters for Solo and removing droplets using
995 a threshold of 0.5. Subsequently, dead / dying cells were filtered by removing droplets with high
996 mitochondrial RNA content (greater than 20% of transcript counts mapped to MT genes) or high
997 ribosomal transcript count (greater than 15% of total transcript counts mapped to ribosomal
998 genes). After pre-processing, poor quality samples with either low numbers of recovered cells or
999 low number of distinct transcripts recovered were removed.

1000

1001 *scRNA-seq normalization and dimensionality reduction*

1002 Filtered count matrices for each sample were combined into a single dataset, normalized to
1003 counts per million (CPM) and log-transformed. Unwanted variation due to total transcript counts
1004 and percentage of mitochondrial reads per cell were regressed out prior to scaling each
1005 transcript to zero mean and unit variance. Principal Component Analysis (PCA) was then
1006 performed on a restricted subset of 5000 highly variable genes using the method described in
1007 (77) and implemented in Scanpy version 1.8.2. The top 50 principal components were kept to
1008 create a UMAP projection (78) using k=10 nearest neighbors to obtain a non-linear 2D
1009 embedding for downstream visualization. Leiden clustering (79) was implemented using Scanpy
1010 version 1.8.2.

1011
1012 The entropy was computed per collection date for each Leiden cluster and revealed 4/42
1013 clusters with more than 100 cells had low batch entropy (< 0.5). Harmony integration was
1014 therefore applied for batch correction (80) using 40 PCs. Reclustered cells verified that post-
1015 integration all Leiden clusters with more than 100 cells had batch entropy > 0.5 .

1016
1017 *scRNA-seq compartment demultiplexing and cell-type assignment*

1018 Cellular compartments were identified from post-integration Leiden clusters using HashSolo (76).
1019 To specifically identify immune cells, we first used hashtag oligonucleotide barcodes matching
1020 FACS-sorted CD45+ populations and all cells clustering with this compartment were included in
1021 the majority label. We manually validated the compartment calls using canonical markers (i.e.
1022 *Ptprc* / CD45 positive; *Vim*, *Col1a2* and *Krt8* negative, for immune cells). A final count of 13,236
1023 (6664 from SEN tumors and 6572 from PRO tumors) CD45 cells and 17,782 genes across 5
1024 samples were recovered and further analyzed using the workflow below.

1025

1026 To define immune subtype clusters, PCA, UMAP projection (with 10 PCs and 10 neighbors),
1027 and Leiden clustering at low resolution (k=10, resolution =0.5) were repeated in immune
1028 compartment cells. Major immune subtypes were annotated by examining top differentially
1029 expressed genes (DEGs) in conjunction with the following marker genes: T-cells and NK cells
1030 (*Cd3e*, *Nkg7*), B-cells (*Cd19*), plasma cells (*Jchain*), granulocytes (*Cxcr2*, *Csf3r*), dendritic cells
1031 (*Clec9a*), monocytes / macrophages (*Cd68*, *Mafb*, *Csf1r*), basophils (*Il3ra*, *Cxcr2*).

1032

1033 Differentially expressed genes were computed by contrasting each Leiden cluster against all
1034 other immune cells using the “rank_gene_groups” function implemented in Scanpy version 1.8.2
1035 using the Wilcoxon rank sum test with Benjamini-Hochberg correction.

1036

1037 This annotation process was repeated on the T/NK-cell subset to characterize the following
1038 phenotypes by marker gene expression: naïve CD4 T-Cells (*Cd4+* *Foxp3-* *Cd69-*), activated
1039 CD4 T-Cells (*Cd4+* *Cd69+*), CD4+ Tregs (*Cd4+* *Foxp3+*), naïve CD8 T-Cells (*Cd8+* *Cd69-*
1040 *Lag3-*), senescent-enriched CD8 T-Cells (*Cd8+* *Cd69+*), proliferating-enriched CD8 T-Cells
1041 (*Cd8+* *Lag3+*), NKT Cells (*Klrb1c+*).

1042

1043 scRNA-seq analysis of T/NK cells

1044 Differential abundance analysis using Milo was performed specifically on T cell subsets (35)
1045 using a neighborhood size of n=50. Differentially abundant T-cell subtypes were identified by
1046 applying the Simes method for multiple hypothesis correction within a subtype cluster or
1047 Benjamini-Hochberg FDR correction across subtypes (setting FDR threshold at 0.2).
1048 Enrichment of a subset of *Cd8+* *Cd69+* T-cells upon p53 reactivation was denoted “Senescent-
1049 enriched CD8 T-cells” and depletion of a subset of *Cd8+* *Cd69+* T-cells was denoted “Growing-
1050 enriched CD8 T-cells”. For visualization purposes, significantly differentially enriched / depleted

1051 neighborhoods by SpatialFDR were visualized as implemented in the MiloPy Python package at
1052 FDR threshold of 0.2.

1053

1054 Differential gene expression analysis within CD8+ T-cell compartment was performed using the
1055 “rank_gene_groups” function as implemented in Python package Scanpy version 1.8.2.
1056 Geneset enrichment analysis using GSEA prerank as implemented in Python package GSEAPy
1057 version 0.12.1. was performed using genes ranked by logFC. Genes were denoted as
1058 differentially expressed using an adjusted p-value cut-off of 0.05 and any human genesets
1059 tested were mapped to corresponding mouse orthologs using Ensembl annotations.

1060

1061 *scRNA-seq analysis of monocyte / macrophages*

1062 Similarly the T/NK-cell analysis, unbiased differential abundance analysis was performed using
1063 Milo as described above, but with a larger neighborhood size of 500 to account for the increase
1064 in cell number in the monocyte / macrophage cluster as well as aggregation at the level of
1065 Leiden clusters, not marker-defined subtypes.

1066

1067 Two Leiden clusters, one significantly enriched and one depleted upon p53 reactivation, were
1068 isolated for differential expression analysis and geneset enrichment as described in the
1069 preceding section and significantly enriched / depleted neighborhoods were visualized using the
1070 same SpatialFDR cut-off of 0.2.

1071

1072 **Statistical analyses**

1073 Statistical analyses were performed as described in the figure legend for each experiment.
1074 Group size was determined on the basis of the results of preliminary experiments, and no
1075 statistical method was used to predetermine sample size. The indicated sample size (n)

1076 represents biological replicates. All samples that met proper experimental conditions were
1077 included in the analysis. In particular, we have observed that in the orthotopic transplantation
1078 setting, the undesired lung metastasis (lung weight > 300 mg) occurred due to the technical
1079 limitation of liver injection. The lung metastasis may affect the tumor regression phenotype upon
1080 p53 restoration, and the mice were thus excluded from the analysis. Survival was measured
1081 using the Kaplan–Meier method. Statistical significance was determined by Student t test, log-
1082 rank test, Mann–Whitney test, Fisher exact test, and Pearson correlation using Prism 6
1083 Software (GraphPad Software) as indicated. Significance was set at $P < 0.05$.

1084

1085 **Figure Preparation**

1086 Figures were prepared using BioRender.com for scientific illustrations and Illustrator CC 2020
1087 (Adobe).

1088

1089 **Data Availability**

1090 RNA-seq data generated in this study are available in the Gene Expression Omnibus (GEO)
1091 database under the super-series GSE203140. The mass spectrometry proteomics data have
1092 been deposited to the ProteomeXchange Consortium via the PRIDE partner repository with the
1093 dataset identifier PXD034465.

1094

1095

1096

1097 **Authors' Contributions**

1098 **Conceptualization and design:** H.-A. Chen, D. Alonso-Curbelo, S.W. Lowe

1099 **Methodology:** H.-A. Chen, R. Mezzadra, J.M. Adrover, C. Zhu, Z. Chen, R.C.

1100 Hendrickson, D. Alonso-Curbelo

1101 **Acquisition and analysis of data (e.g., investigation, validation, resources):** H.-A,

1102 Chen, R. Mezzadra, J.M. Adrover, C. Zhu, W. Luan, A. Wuest, S. Tian, K Woess, C

1103 Broderick, X. Li, N. Bernstein, G. Schmitt, L. Fong, Z. Chen, R.C. Hendrickson, M.

1104 Egeblad, D. Alonso-Curbelo

1105 **Formal analysis and software:** Y.-J. Ho, J.M. Adrover, N. Bernstein, G. Schmitt, Z.

1106 Chen, R.C. Hendrickson

1107 **Writing—original draft presentation:** H.-A, Chen, D. Alonso-Curbelo, S.W. Lowe

1108 **Writing—review and editing:** H.-A, Chen, Y.-J. Ho, R. Mezzadra, J.M. Adrover, C. Zhu,

1109 L. Fong, Z. Chen, M. Egeblad, D. Alonso-Curbelo, S.W. Lowe

1110 **Visualization:** H.-A, Chen, Y.-J. Ho, J.M. Adrover, Z. Chen, D. Alonso-Curbelo

1111 **Study supervision:** D. Alonso-Curbelo, S.W. Lowe

1112 **Acknowledgments**

1113 We thank J. Simon and the MSKCC animal facility for technical support with animal

1114 colonies; J.E. Wilkinson and J. Shia for mouse liver cancer pathology consulting; E. de

1115 Stanchina and A. Kulick from the MSKCC Antitumor Assessment Core Facility for

1116 animal treatment support; Z. Li, A. Gaito and M. Miele from the MSKCC Microchemistry

1117 & Proteomics core for proteomic profiling technical support; N. Prats and M. Aguilera

1118 from the IRB Barcelona Histopathology Facility for the support of immunofluorescence

1119 staining protocol; and J.P. Morris IV, S. Houlihan, J. Novak and other members of the

1120 Lowe laboratory for advice, paper editing and discussions. H.-A. Chen was supported
1121 by a NIH F99 Fellowship (F99CA245797). D. Alonso-Curbelo is supported by the “*la*
1122 *Caixa*” Foundation Junior Leader Fellowship (LCF/BQ/PI20/11760006). R. Mezzadra
1123 was supported by NWO (Dutch Research Council- Rubicon Fellowship 452182318) and
1124 is a Cancer Research Institute Irvington Fellow supported by the Cancer Research
1125 Institute (CRI Award #3441). J.M. Adrover is the recipient of a Cancer Research
1126 Institute/Irvington Postdoctoral Fellowship (CRI Award #3435). C. Zhu is supported by
1127 an F32 Postdoctoral Fellowship (1F32CA257103) from the NIH/NCI. M. Egeblad is
1128 supported by a grant from the National Cancer Institute (1R01CA237413) and the work
1129 was supported by the Cold Spring Harbor Laboratory (CSHL) Cancer Center
1130 (P30CA045508). This work was also supported by the IRB Barcelona and “*la Caixa*”
1131 Foundation (to D. Alonso-Curbelo); and the NIH/NCI P01CA087497 and Calico Life
1132 Sciences grants (to S.W. Lowe). S.W. Lowe is an investigator in the Howard Hughes
1133 Medical Institute and the Geoffrey Beene Chair for Cancer Biology.

1134
1135

1136 REFERENCES

- 1137 1. Di Micco R, Krizhanovsky V, Baker D, d'Adda di Fagagna F. Cellular senescence in
1138 ageing: from mechanisms to therapeutic opportunities. *Nat Rev Mol Cell Biol*
1139 **2021**;22(2):75-95 doi 10.1038/s41580-020-00314-w.
- 1140 2. Munoz-Espin D, Serrano M. Cellular senescence: from physiology to pathology. *Nat Rev*
1141 *Mol Cell Biol* **2014**;15(7):482-96 doi 10.1038/nrm3823.
- 1142 3. Demaria M, Ohtani N, Youssef SA, Rodier F, Toussaint W, Mitchell JR, *et al.* An
1143 essential role for senescent cells in optimal wound healing through secretion of PDGF-
1144 AA. *Dev Cell* **2014**;31(6):722-33 doi 10.1016/j.devcel.2014.11.012.
- 1145 4. Xu M, Pirtskhalava T, Farr JN, Weigand BM, Palmer AK, Weivoda MM, *et al.* Senolytics
1146 improve physical function and increase lifespan in old age. *Nat Med* **2018**;24(8):1246-56
1147 doi 10.1038/s41591-018-0092-9.
- 1148 5. Serrano M, Lin AW, McCurrach ME, Beach D, Lowe SW. Oncogenic ras provokes
1149 premature cell senescence associated with accumulation of p53 and p16INK4a. *Cell*
1150 **1997**;88(5):593-602 doi 10.1016/s0092-8674(00)81902-9.
- 1151 6. Ewald JA, Desotelle JA, Wilding G, Jarrard DF. Therapy-induced senescence in cancer.
1152 *Journal of the National Cancer Institute* **2010**;102(20):1536-46 doi 10.1093/jnci/djq364.
- 1153 7. Coppe JP, Desprez PY, Krtolica A, Campisi J. The senescence-associated secretory
1154 phenotype: the dark side of tumor suppression. *Annu Rev Pathol* **2010**;5:99-118 doi
1155 10.1146/annurev-pathol-121808-102144.
- 1156 8. Demaria M, O'Leary MN, Chang J, Shao L, Liu S, Alimirah F, *et al.* Cellular Senescence
1157 Promotes Adverse Effects of Chemotherapy and Cancer Relapse. *Cancer Discov*
1158 **2017**;7(2):165-76 doi 10.1158/2159-8290.CD-16-0241.
- 1159 9. Coppe JP, Patil CK, Rodier F, Sun Y, Munoz DP, Goldstein J, *et al.* Senescence-
1160 associated secretory phenotypes reveal cell-nonautonomous functions of oncogenic
1161 RAS and the p53 tumor suppressor. *PLoS biology* **2008**;6(12):2853-68 doi
1162 10.1371/journal.pbio.0060301.
- 1163 10. Tasdemir N, Banito A, Roe JS, Alonso-Curbelo D, Camiolo M, Tschaharganeh DF, *et al.*
1164 BRD4 Connects Enhancer Remodeling to Senescence Immune Surveillance. *Cancer*
1165 *Discov* **2016**;6(6):612-29 doi 10.1158/2159-8290.CD-16-0217.
- 1166 11. Chien Y, Scuoppo C, Wang X, Fang X, Balgley B, Bolden JE, *et al.* Control of the
1167 senescence-associated secretory phenotype by NF-kappaB promotes senescence and
1168 enhances chemosensitivity. *Genes Dev* **2011**;25(20):2125-36 doi
1169 10.1101/gad.17276711.
- 1170 12. Kuilman T, Michaloglou C, Vredeveld LC, Douma S, van Doorn R, Desmet CJ, *et al.*
1171 Oncogene-induced senescence relayed by an interleukin-dependent inflammatory
1172 network. *Cell* **2008**;133(6):1019-31 doi 10.1016/j.cell.2008.03.039.
- 1173 13. Basisty N, Kale A, Jeon OH, Kuehnemann C, Payne T, Rao C, *et al.* A proteomic atlas of
1174 senescence-associated secretomes for aging biomarker development. *PLoS biology*
1175 **2020**;18(1):e3000599 doi 10.1371/journal.pbio.3000599.
- 1176 14. Hernandez-Segura A, de Jong TV, Melov S, Guryev V, Campisi J, Demaria M.
1177 Unmasking Transcriptional Heterogeneity in Senescent Cells. *Curr Biol*
1178 **2017**;27(17):2652-60 e4 doi 10.1016/j.cub.2017.07.033.
- 1179 15. Xue W, Zender L, Miething C, Dickins RA, Hernando E, Krizhanovsky V, *et al.*
1180 Senescence and tumour clearance is triggered by p53 restoration in murine liver
1181 carcinomas. *Nature* **2007**;445(7128):656-60 doi 10.1038/nature05529.
- 1182 16. Kang TW, Yevsa T, Woller N, Hoenicke L, Wuestefeld T, Dauch D, *et al.* Senescence
1183 surveillance of pre-malignant hepatocytes limits liver cancer development. *Nature*
1184 **2011**;479(7374):547-51 doi 10.1038/nature10599.

- 1185 17. Ovadya Y, Landsberger T, Leins H, Vadai E, Gal H, Biran A, *et al.* Impaired immune
1186 surveillance accelerates accumulation of senescent cells and aging. *Nat Commun*
1187 **2018**;9(1):5435 doi 10.1038/s41467-018-07825-3.
- 1188 18. Lujambio A. To clear, or not to clear (senescent cells)? That is the question. *Bioessays*
1189 **2016**;38 Suppl 1:S56-64 doi 10.1002/bies.201670910.
- 1190 19. Di Mitri D, Toso A, Chen JJ, Sarti M, Pinton S, Jost TR, *et al.* Tumour-infiltrating Gr-1+
1191 myeloid cells antagonize senescence in cancer. *Nature* **2014**;515(7525):134-7 doi
1192 10.1038/nature13638.
- 1193 20. Ruscetti M, Leibold J, Bott MJ, Fennell M, Kulick A, Salgado NR, *et al.* NK cell-mediated
1194 cytotoxicity contributes to tumor control by a cytostatic drug combination. *Science*
1195 **2018**;362(6421):1416-22 doi 10.1126/science.aas9090.
- 1196 21. Llovet JM, Kelley RK, Villanueva A, Singal AG, Pikarsky E, Roayaie S, *et al.*
1197 Hepatocellular carcinoma. *Nat Rev Dis Primers* **2021**;7(1):6 doi 10.1038/s41572-020-
1198 00240-3.
- 1199 22. Chiang DY, Villanueva A, Hoshida Y, Peix J, Newell P, Minguez B, *et al.* Focal gains of
1200 VEGFA and molecular classification of hepatocellular carcinoma. *Cancer Res*
1201 **2008**;68(16):6779-88 doi 10.1158/0008-5472.CAN-08-0742.
- 1202 23. Llovet JM, Castet F, Heikenwalder M, Maini MK, Mazzaferro V, Pinato DJ, *et al.*
1203 Immunotherapies for hepatocellular carcinoma. *Nat Rev Clin Oncol* **2022**;19(3):151-72
1204 doi 10.1038/s41571-021-00573-2.
- 1205 24. Sangro B, Sarobe P, Hervas-Stubbs S, Melero I. Advances in immunotherapy for
1206 hepatocellular carcinoma. *Nat Rev Gastroenterol Hepatol* **2021**;18(8):525-43 doi
1207 10.1038/s41575-021-00438-0.
- 1208 25. Levine AJ. Targeting the P53 Protein for Cancer Therapies: The Translational Impact of
1209 P53 Research. *Cancer Res* **2022**;82(3):362-4 doi 10.1158/0008-5472.CAN-21-2709.
- 1210 26. Xiao Y, Chen J, Zhou H, Zeng X, Ruan Z, Pu Z, *et al.* Combining p53 mRNA
1211 nanotherapy with immune checkpoint blockade reprograms the immune
1212 microenvironment for effective cancer therapy. *Nat Commun* **2022**;13(1):758 doi
1213 10.1038/s41467-022-28279-8.
- 1214 27. Demir O, Barros EP, Offutt TL, Rosenfeld M, Amaro RE. An integrated view of p53
1215 dynamics, function, and reactivation. *Curr Opin Struct Biol* **2021**;67:187-94 doi
1216 10.1016/j.sbi.2020.11.005.
- 1217 28. Suda T, Liu D. Hydrodynamic gene delivery: its principles and applications. *Mol Ther*
1218 **2007**;15(12):2063-9 doi 10.1038/sj.mt.6300314.
- 1219 29. Hoshida Y, Nijman SM, Kobayashi M, Chan JA, Brunet JP, Chiang DY, *et al.* Integrative
1220 transcriptome analysis reveals common molecular subclasses of human hepatocellular
1221 carcinoma. *Cancer Res* **2009**;69(18):7385-92 doi 10.1158/0008-5472.CAN-09-1089.
- 1222 30. Kaech SM, Hemby S, Kersh E, Ahmed R. Molecular and functional profiling of memory
1223 CD8 T cell differentiation. *Cell* **2002**;111(6):837-51 doi 10.1016/s0092-8674(02)01139-x.
- 1224 31. Bruix J, Cheng AL, Meinhardt G, Nakajima K, De Sanctis Y, Llovet J. Prognostic factors
1225 and predictors of sorafenib benefit in patients with hepatocellular carcinoma: Analysis of
1226 two phase III studies. *J Hepatol* **2017**;67(5):999-1008 doi 10.1016/j.jhep.2017.06.026.
- 1227 32. Adrover JM, Aroca-Crevillen A, Crainiciuc G, Ostos F, Rojas-Vega Y, Rubio-Ponce A, *et al.*
1228 Programmed 'disarming' of the neutrophil proteome reduces the magnitude of
1229 inflammation. *Nat Immunol* **2020**;21(2):135-44 doi 10.1038/s41590-019-0571-2.
- 1230 33. Zeisberger SM, Odermatt B, Marty C, Zehnder-Fjallman AH, Ballmer-Hofer K,
1231 Schwendener RA. Clodronate-liposome-mediated depletion of tumour-associated
1232 macrophages: a new and highly effective antiangiogenic therapy approach. *Br J Cancer*
1233 **2006**;95(3):272-81 doi 10.1038/sj.bjc.6603240.
- 1234 34. De Simone G, Andreatta F, Bleriot C, Fumagalli V, Laura C, Garcia-Manteiga JM, *et al.*
1235 Identification of a Kupffer cell subset capable of reverting the T cell dysfunction induced

- 1236 by hepatocellular priming. *Immunity* **2021**;54(9):2089-100 e8 doi
 1237 10.1016/j.immuni.2021.05.005.
- 1238 35. Dann E, Henderson NC, Teichmann SA, Morgan MD, Marioni JC. Differential
 1239 abundance testing on single-cell data using k-nearest neighbor graphs. *Nat Biotechnol*
 1240 **2022**;40(2):245-53 doi 10.1038/s41587-021-01033-z.
- 1241 36. Kim HD, Park S, Jeong S, Lee YJ, Lee H, Kim CG, *et al.* 4-1BB Delineates Distinct
 1242 Activation Status of Exhausted Tumor-Infiltrating CD8(+) T Cells in Hepatocellular
 1243 Carcinoma. *Hepatology* **2020**;71(3):955-71 doi 10.1002/hep.30881.
- 1244 37. Li Y, Wang Z, Jiang W, Zeng H, Liu Z, Lin Z, *et al.* Tumor-infiltrating TNFRSF9(+) CD8(+)
 1245 T cells define different subsets of clear cell renal cell carcinoma with prognosis and
 1246 immunotherapeutic response. *Oncoimmunology* **2020**;9(1):1838141 doi
 1247 10.1080/2162402X.2020.1838141.
- 1248 38. Bindea G, Mlecnik B, Tosolini M, Kirilovsky A, Waldner M, Obenauf AC, *et al.*
 1249 Spatiotemporal dynamics of intratumoral immune cells reveal the immune landscape in
 1250 human cancer. *Immunity* **2013**;39(4):782-95 doi 10.1016/j.immuni.2013.10.003.
- 1251 39. Kuang DM, Zhao Q, Peng C, Xu J, Zhang JP, Wu C, *et al.* Activated monocytes in
 1252 peritumoral stroma of hepatocellular carcinoma foster immune privilege and disease
 1253 progression through PD-L1. *J Exp Med* **2009**;206(6):1327-37 doi 10.1084/jem.20082173.
- 1254 40. Lu LG, Zhou ZL, Wang XY, Liu BY, Lu JY, Liu S, *et al.* PD-L1 blockade liberates intrinsic
 1255 antitumorigenic properties of glycolytic macrophages in hepatocellular carcinoma. *Gut*
 1256 **2022** doi 10.1136/gutjnl-2021-326350.
- 1257 41. Milanovic M, Fan DNY, Belenki D, Dabritz JHM, Zhao Z, Yu Y, *et al.* Senescence-
 1258 associated reprogramming promotes cancer stemness. *Nature* **2018**;553(7686):96-100
 1259 doi 10.1038/nature25167.
- 1260 42. Yousef H, Czupalla CJ, Lee D, Chen MB, Burke AN, Zera KA, *et al.* Aged blood impairs
 1261 hippocampal neural precursor activity and activates microglia via brain endothelial cell
 1262 VCAM1. *Nat Med* **2019**;25(6):988-1000 doi 10.1038/s41591-019-0440-4.
- 1263 43. Rapisarda V, Borghesan M, Miguela V, Encheva V, Snijders AP, Lujambio A, *et al.*
 1264 Integrin Beta 3 Regulates Cellular Senescence by Activating the TGF-beta Pathway.
 1265 *Cell Rep* **2017**;18(10):2480-93 doi 10.1016/j.celrep.2017.02.012.
- 1266 44. Jochems F, Thijssen B, De Conti G, Jansen R, Pogacar Z, Groot K, *et al.* The Cancer
 1267 SENESCopedia: A delineation of cancer cell senescence. *Cell Rep* **2021**;36(4):109441
 1268 doi 10.1016/j.celrep.2021.109441.
- 1269 45. Perna F, Berman SH, Soni RK, Mansilla-Soto J, Eyquem J, Hamieh M, *et al.* Integrating
 1270 Proteomics and Transcriptomics for Systematic Combinatorial Chimeric Antigen
 1271 Receptor Therapy of AML. *Cancer Cell* **2017**;32(4):506-19 e5 doi
 1272 10.1016/j.ccell.2017.09.004.
- 1273 46. Hoare M, Ito Y, Kang TW, Weekes MP, Matheson NJ, Patten DA, *et al.* NOTCH1
 1274 mediates a switch between two distinct secretomes during senescence. *Nat Cell Biol*
 1275 **2016**;18(9):979-92 doi 10.1038/ncb3397.
- 1276 47. Castro F, Cardoso AP, Goncalves RM, Serre K, Oliveira MJ. Interferon-Gamma at the
 1277 Crossroads of Tumor Immune Surveillance or Evasion. *Front Immunol* **2018**;9:847 doi
 1278 10.3389/fimmu.2018.00847.
- 1279 48. Plataniias LC. Mechanisms of type-I- and type-II-interferon-mediated signalling. *Nat Rev*
 1280 *Immunol* **2005**;5(5):375-86 doi 10.1038/nri1604.
- 1281 49. Manguso RT, Pope HW, Zimmer MD, Brown FD, Yates KB, Miller BC, *et al.* In vivo
 1282 CRISPR screening identifies Ptpn2 as a cancer immunotherapy target. *Nature*
 1283 **2017**;547(7664):413-8 doi 10.1038/nature23270.
- 1284 50. Song MM, Shuai K. The suppressor of cytokine signaling (SOCS) 1 and SOCS3 but not
 1285 SOCS2 proteins inhibit interferon-mediated antiviral and antiproliferative activities. *J Biol*
 1286 *Chem* **1998**;273(52):35056-62 doi 10.1074/jbc.273.52.35056.

- 1287 51. Kleppe M, Soulier J, Asnafi V, Mentens N, Hornakova T, Knoop L, *et al.* PTPN2
1288 negatively regulates oncogenic JAK1 in T-cell acute lymphoblastic leukemia. *Blood*
1289 **2011**;117(26):7090-8 doi 10.1182/blood-2010-10-314286.
- 1290 52. Zhou F. Molecular mechanisms of IFN-gamma to up-regulate MHC class I antigen
1291 processing and presentation. *Int Rev Immunol* **2009**;28(3-4):239-60 doi
1292 10.1080/08830180902978120.
- 1293 53. McCarthy MK, Weinberg JB. The immunoproteasome and viral infection: a complex
1294 regulator of inflammation. *Front Microbiol* **2015**;6:21 doi 10.3389/fmicb.2015.00021.
- 1295 54. Yoshihama S, Vijayan S, Sidiq T, Kobayashi KS. NLRC5/CITA: A Key Player in Cancer
1296 Immune Surveillance. *Trends Cancer* **2017**;3(1):28-38 doi 10.1016/j.trecan.2016.12.003.
- 1297 55. Kalaora S, Lee JS, Barnea E, Levy R, Greenberg P, Alon M, *et al.* Immunoproteasome
1298 expression is associated with better prognosis and response to checkpoint therapies in
1299 melanoma. *Nat Commun* **2020**;11(1):896 doi 10.1038/s41467-020-14639-9.
- 1300 56. Efeyan A, Ortega-Molina A, Velasco-Miguel S, Herranz D, Vassilev LT, Serrano M.
1301 Induction of p53-dependent senescence by the MDM2 antagonist nutlin-3a in mouse
1302 cells of fibroblast origin. *Cancer Res* **2007**;67(15):7350-7 doi 10.1158/0008-5472.CAN-
1303 07-0200.
- 1304 57. Hoekstra ME, Bornes L, Dijkgraaf FE, Philips D, Pardieck IN, Toebes M, *et al.* Long-
1305 distance modulation of bystander tumor cells by CD8(+) T cell-secreted IFNgamma. *Nat*
1306 *Cancer* **2020**;1(3):291-301 doi 10.1038/s43018-020-0036-4.
- 1307 58. Ruscetti M, Morris JPt, Mezzadra R, Russell J, Leibold J, Romesser PB, *et al.*
1308 Senescence-Induced Vascular Remodeling Creates Therapeutic Vulnerabilities in
1309 Pancreas Cancer. *Cell* **2020**;181(2):424-41 e21 doi 10.1016/j.cell.2020.03.008.
- 1310 59. Dighe AS, Richards E, Old LJ, Schreiber RD. Enhanced in vivo growth and resistance to
1311 rejection of tumor cells expressing dominant negative IFN gamma receptors. *Immunity*
1312 **1994**;1(6):447-56 doi 10.1016/1074-7613(94)90087-6.
- 1313 60. Gao J, Shi LZ, Zhao H, Chen J, Xiong L, He Q, *et al.* Loss of IFN-gamma Pathway
1314 Genes in Tumor Cells as a Mechanism of Resistance to Anti-CTLA-4 Therapy. *Cell*
1315 **2016**;167(2):397-404 e9 doi 10.1016/j.cell.2016.08.069.
- 1316 61. Paffenholz SV, Salvagno C, Ho YJ, Limjoco M, Baslan T, Tian S, *et al.* Senescence
1317 induction dictates response to chemo- and immunotherapy in preclinical models of
1318 ovarian cancer. *Proc Natl Acad Sci U S A* **2022**;119(5) doi 10.1073/pnas.2117754119.
- 1319 62. Shao DD, Xue W, Krall EB, Bhutkar A, Piccioni F, Wang X, *et al.* KRAS and YAP1
1320 converge to regulate EMT and tumor survival. *Cell* **2014**;158(1):171-84 doi
1321 10.1016/j.cell.2014.06.004.
- 1322 63. Zhu C, Kim K, Wang X, Bartolome A, Salomao M, Dongiovanni P, *et al.* Hepatocyte
1323 Notch activation induces liver fibrosis in nonalcoholic steatohepatitis. *Sci Transl Med*
1324 **2018**;10(468) doi 10.1126/scitranslmed.aat0344.
- 1325 64. Susaki EA, Tainaka K, Perrin D, Yukinaga H, Kuno A, Ueda HR. Advanced CUBIC
1326 protocols for whole-brain and whole-body clearing and imaging. *Nat Protoc*
1327 **2015**;10(11):1709-27 doi 10.1038/nprot.2015.085.
- 1328 65. Bolger AM, Lohse M, Usadel B. Trimmomatic: a flexible trimmer for Illumina sequence
1329 data. *Bioinformatics* **2014**;30(15):2114-20 doi 10.1093/bioinformatics/btu170.
- 1330 66. Dobin A, Davis CA, Schlesinger F, Drenkow J, Zaleski C, Jha S, *et al.* STAR: ultrafast
1331 universal RNA-seq aligner. *Bioinformatics* **2013**;29(1):15-21 doi
1332 10.1093/bioinformatics/bts635.
- 1333 67. Anders S, Pyl PT, Huber W. HTSeq--a Python framework to work with high-throughput
1334 sequencing data. *Bioinformatics* **2015**;31(2):166-9 doi 10.1093/bioinformatics/btu638.
- 1335 68. Love MI, Huber W, Anders S. Moderated estimation of fold change and dispersion for
1336 RNA-seq data with DESeq2. *Genome Biol* **2014**;15(12):550 doi 10.1186/s13059-014-
1337 0550-8.

- 1338 69. Chen EY, Tan CM, Kou Y, Duan Q, Wang Z, Meirelles GV, *et al.* Enrichr: interactive and
1339 collaborative HTML5 gene list enrichment analysis tool. *BMC Bioinformatics*
1340 **2013**;14:128 doi 10.1186/1471-2105-14-128.
- 1341 70. Foroutan M, Bhuva DD, Lyu R, Horan K, Cursons J, Davis MJ. Single sample scoring of
1342 molecular phenotypes. *BMC Bioinformatics* **2018**;19(1):404 doi 10.1186/s12859-018-
1343 2435-4.
- 1344 71. Binder JX, Pletscher-Frankild S, Tsafou K, Stolte C, O'Donoghue SI, Schneider R, *et al.*
1345 COMPARTMENTS: unification and visualization of protein subcellular localization
1346 evidence. *Database (Oxford)* **2014**;2014:bau012 doi 10.1093/database/bau012.
- 1347 72. Cancer Genome Atlas Research Network. Electronic address wbe, Cancer Genome
1348 Atlas Research N. Comprehensive and Integrative Genomic Characterization of
1349 Hepatocellular Carcinoma. *Cell* **2017**;169(7):1327-41 e23 doi 10.1016/j.cell.2017.05.046.
- 1350 73. Colaprico A, Silva TC, Olsen C, Garofano L, Cava C, Garolini D, *et al.* TCGAbiolinks: an
1351 R/Bioconductor package for integrative analysis of TCGA data. *Nucleic Acids Res*
1352 **2016**;44(8):e71 doi 10.1093/nar/gkv1507.
- 1353 74. Hanzelmann S, Castelo R, Guinney J. GSVA: gene set variation analysis for microarray
1354 and RNA-seq data. *BMC Bioinformatics* **2013**;14:7 doi 10.1186/1471-2105-14-7.
- 1355 75. Bankhead P, Loughrey MB, Fernandez JA, Dombrowski Y, McArt DG, Dunne PD, *et al.*
1356 QuPath: Open source software for digital pathology image analysis. *Sci Rep*
1357 **2017**;7(1):16878 doi 10.1038/s41598-017-17204-5.
- 1358 76. Bernstein NJ, Fong NL, Lam I, Roy MA, Hendrickson DG, Kelley DR. Solo: Doublet
1359 Identification in Single-Cell RNA-Seq via Semi-Supervised Deep Learning. *Cell Syst*
1360 **2020**;11(1):95-101 e5 doi 10.1016/j.cels.2020.05.010.
- 1361 77. Satija R, Farrell JA, Gennert D, Schier AF, Regev A. Spatial reconstruction of single-cell
1362 gene expression data. *Nat Biotechnol* **2015**;33(5):495-502 doi 10.1038/nbt.3192.
- 1363 78. McInnes L, Healy J, Melville J. UMAP: Uniform Manifold Approximation and Projection
1364 for Dimension Reduction. *arXiv* **2018**:doi: 10.48550/ARXIV.1802.03426.
- 1365 79. Traag VA, Waltman L, van Eck NJ. From Louvain to Leiden: guaranteeing well-
1366 connected communities. *Sci Rep* **2019**;9(1):5233 doi 10.1038/s41598-019-41695-z.
- 1367 80. Korsunsky I, Millard N, Fan J, Slowikowski K, Zhang F, Wei K, *et al.* Fast, sensitive and
1368 accurate integration of single-cell data with Harmony. *Nat Methods* **2019**;16(12):1289-96
1369 doi 10.1038/s41592-019-0619-0.
- 1370
1371
1372
1373

1374 **MAIN FIGURE LEGENDS**

1375 **Figure 1. A p53-restorable tumor model to study senescence immune surveillance**

1376 A, Generation of the p53-restorable, NRAS-driven mouse liver cancer model using the sleeping
1377 beauty transposon system delivered through hydrodynamic tail vein injection (HTVI). (Created
1378 with BioRender.com.)

1379 B, Representative ultrasonogram of HTVI and orthotopic injection liver cancer models at
1380 indicated time after p53 restoration.

1381 C, Survival analysis of mice in the HTVI model.

1382 D, Representative hematoxylin and eosin (H&E), immunofluorescence (IF) and senescence-
1383 associated β -Gal (SA- β -Gal) staining of p53-suppressed (p53 Off) and -restored (p53 On for 14
1384 days) tumor sections generated from the HTVI model. Scale bar, 50 μ m.

1385 E to G, Orthotopic injection of GFP-luciferase vector-transduced NSP tumor cells into the livers
1386 of immunocompetent and -deficient mouse strains.

1387 E, Tumor size change measured by ultrasound upon p53 restoration. R2G2, Rag2-Il2rg double
1388 knockout mouse. Data are presented as mean \pm s.e.m. $N \geq 9$ for each strain.

1389 F, Representative macroscopic pictures at 21 days of p53 On or end-point p53 Off tumor.

1390 G, Representative immunohistochemistry (IHC) staining of GFP-labeled tumor cells at day 21
1391 upon p53 restoration. Scale bar, 100 μ m.

1392

1393 **Figure 2. Senescence triggers an immune evasion-to-immune recognition tumor switch**

1394 A, Representative images of CD45 and GFP staining marking immune cells and tumor cells,
1395 respectively in p53-suppressed and p53-restored tumor (7 days after p53 restoration). Right
1396 panel is the quantification of the area of CD45+ staining calculated from 3 random fields per
1397 mouse. Each dot represents a mouse.

1398 B, Flow cytometry analysis of global immune landscape in orthotopic NSP liver tumor model.

1399 Immunophenotyping of senescent tumors is performed 9 days after Dox withdrawal, a time point

1400 when the senescent state is fully established yet, preceding the massive tumor regression. G-
1401 MDSC, granulocytic myeloid-derived suppressor cells. M-MDSC, monocytic myeloid-derived
1402 suppressor cells. Data is pooled from 2 independent experiments with n=7 in the proliferating
1403 group and n=9 in the senescent group. Note that, as absolute number of CD45+ cells increases
1404 in senescent NSP tumor lesions (A), so do the total numbers of the indicated cell types.
1405 C, Flow cytometry analysis of CD8 T cells. Data is pooled from 2 independent experiments with
1406 n=11 in the proliferating and n=10 in the senescent groups. Experiments were performed at 9
1407 days after Dox withdrawal.
1408 D, Representative tissue clearing images of the orthotopic NSP liver tumors. T cells, neutrophils
1409 and vasculature are labeled by CD3, MPO and CD31 staining, respectively. Samples were
1410 collected at 9 days after Dox withdrawal.
1411 E, Tumor size change measured by ultrasound upon p53 restoration in mice after depleting
1412 specific immune cell types using antibodies or drugs.
1413 F, Left panel, UMAP plot of CD8+ T cells isolated from p53-suppressed proliferating (PRO) and
1414 p53-reactivated senescent (SEN) tumors. Right panel, GSEA of a T cell exhaustion marker
1415 genes in CD8+ T cells from proliferating (p53-suppressed) vs senescent (p53-reactivated)
1416 tumors.
1417 G, UMAP plot of the expression of selected genes (*Cd8a*, *Cd44*, *Tnfrsf9*, *Cd69*, *Tox*, *Fasl*)
1418 between CD8+ T cells isolated from senescent (p53-reactivated) and proliferating (p53-
1419 suppressed) tumors.
1420 H, Representative immunofluorescence images of CD8 T cells and F4/80 positive macrophages
1421 staining in the orthotopic NSP liver tumor. Tumor samples were collected at 9 days after Dox
1422 withdrawal.
1423 Data is presented as mean \pm s.e.m. Scale bar, 100 μ m. A two-tailed student t-test is used. *p <
1424 0.05; **p < 0.01.
1425

1426 **Figure 3. Senescence remodels tissue sensing programs and cell-surfaceome landscape**

1427 A, GSEA (Reactome) of RNA-Seq data from proliferating (PRO, p53 Off) vs. senescent (SEN,
1428 p53 On for 8 days) NSP liver tumor cells *in vitro*.

1429 B, Subcellular localization of DEGs ($p < 0.05$; fold change > 2) all detected genes (TPM > 1)
1430 from RNA-seq.

1431 C, Gene Ontology (GO) analysis of DEGs encoding plasma membrane proteins upregulated in
1432 senescent cells.

1433 D, Transcriptomic analysis of all differential expressed genes (DEGs, proliferating vs. senescent)
1434 in the presence or absence JQ1 treatment. C1 cluster (in red) contains the senescence-specific
1435 genes sensitive to JQ1 and C4 cluster (in blue) contains the proliferation-specific genes
1436 sensitive to JQ1.

1437 E, Meta-analysis of RNA-seq datasets from SENESCOPEDIA by performing subcellular
1438 localization of DEGs (same as Fig. 2D) and Fisher exact test to examine the relative enrichment
1439 of up- and downregulated EC/PM-DEGs deviated from the random distribution. See also
1440 Supplementary Fig. S7E and S7F.

1441 F, Mass spectrometry (MS) analysis of plasma membrane-enriched proteome in proliferating
1442 and senescent cells. Protein level is normalized to mean expression of the protein of all samples.
1443 Controls are the samples without biotin labeling serving as background. Red and blue boxes
1444 represent proteins enriched in senescent and proliferating cells respectively. N=6 for both
1445 senescent and proliferating experimental group, and N=3 and 4 respectively for their control.

1446 G, Distribution of up- and downregulated Genecard-annotated plasma membrane (PM) proteins
1447 profiled by MS.

1448 H, Volcano plot of Genecard-annotated plasma membrane proteins profiled by MS.

1449 EC, extracellular; PM, plasma membrane.

1450

1451 **Figure 4. Senescent cells are primed to sense and amplify IFN- γ signaling**

1452 A and B, IFNGR1 level on proliferating and senescent cells profiled by mass spectrometry and
1453 validated by flow cytometry (B). AU, arbitrary unit. Data is presented as mean \pm s.e.m. n = 6 for
1454 both proliferating and senescent group.

1455 C, Transcriptomic analysis of selected genes regulating IFN- γ signaling from RNA-seq data of 3
1456 independent p53-restorable cell lines (NSP, NSM2, NSP5) restoring p53 along with NSP cells
1457 treated with two other senescence triggers. T+P, trametinib plus palbociclib.

1458 D, mRNA expression of selected genes involved in IFN- γ signaling in human cell lines triggered
1459 to senesce. Treatment: Ali, alisertib; Eto, etoposide; number indicates the length of treatment
1460 (days). Data is obtained from the public dataset SENESCOPEDIA (44).

1461 E, Top panel, immunoblot analysis of NSP cells under different senescent triggers, in presence
1462 or absence of IFN- γ (1 ng/ml). Bottom panel, quantification of the intensity of signal from
1463 immunoblot. p-Stat1, phospho-Stat1 (Tyr701).

1464
1465 **Figure 5. Senescence and extracellular IFN- γ cooperate to upregulate antigen processing**
1466 **and presentation machinery**

1467 A and B, mRNA expression of genes in proliferating and senescent NSP cells *in vitro* in the
1468 presence or absence of IFN- γ (50 pg/ml) treatment. mRNA level is normalized to the mean
1469 expression of the gene in all samples. A, differential expressed genes encoding SASP factors in
1470 our model. B, IFN- γ response genes from Hallmark signature database.

1471 C, RT-qPCR of selected antigen presentation pathway genes in proliferating and senescent
1472 cells treated with low (50 pg/ml) or high (1 ng/ml) concentration of IFN- γ . Samples are from 2
1473 biological replicates.

1474 D, MHC-I level of proliferating and senescent cells treated with IFN- γ for 24 hours measured by
1475 flow cytometer.

1476 MFI, median fluorescence intensity. Data is presented as mean \pm s.e.m.

1477

1478 **Figure 6. Senescence enhances IFN- γ -mediated heterotypic signaling from activated**
1479 **immune cells to tumor cells**

1480 A, Graphic illustration of IFN- γ sensing (IGS) reporter. (Created with [BioRender.com](https://www.biorender.com).)

1481 B, Left panel, representative flow cytometry plots measuring ZsGreen1 signals in proliferating
1482 and senescent NSP cells treated with 1 ng/ml IFN- γ . Right panel, quantification of the
1483 percentage of ZsGreen1 positive cells upon IFN- γ treatment.

1484 C and D, Representative 3D imaging of tissue cleared tumors from the orthotopically injected
1485 liver NSP cell line expressing IGS reporter (C). Quantification of 3 randomly selected fields from
1486 the liver tumor of each mouse (D). N=5 and N=3 for the proliferating and senescent group (9
1487 days after p53 restoration) respectively.

1488 E, Top panel, cytometric bead array (CBA) assay for IFN- γ level from *in vivo* tumor tissue lysate
1489 samples (7 days after p53 restoration). Bottom panel, Transcripts of indicated genes from RNA-
1490 seq of *in vivo* bulk samples of tumors generated by HTVI (PRO, p53 Off; SEN, p53 restoration
1491 for 12 days). TPM, Transcripts Per Kilobase Million. Noted *Ifna/b* cluster contains 14 *Ifna*
1492 subtypes and 1 *Ifnb* gene.

1493 F and G, Expression of *Ifng* in tumor infiltrating immune cells profiled by scRNA-seq in NSP
1494 transplantable model (as in Figure 2, sample collected at day 8 after p53 restoration).

1495 H, UMAP plot of the expression of *Havcr2* (encoding TIM-3) and *Ifng* in CD8 T cells harvested
1496 from proliferating (P) and senescent (S) tumor lesion. Top panel is replicated from Figure 2F
1497 (left) to indicate cells corresponding to each condition.

1498 I, Quantification of ZsGreen1 intensity of NSP tumor cells in the OT-I T cells and SIINFEKL-
1499 expressing tumor cells co-culture experiment (E/T ratio 5:1) after 20 h of co-culture. Signal
1500 measured by flow cytometry. T+P, trametinib plus palbociclib. See experimental details in
1501 supplementary Fig. S12E.

1502 MFI, median fluorescence intensity. Data is presented as mean \pm s.e.m. Two-tailed student t-
1503 test is used. *p < 0.05. Scale bar, 100 μ m.

1504
1505
1506
1507
1508
1509
1510
1511
1512
1513
1514
1515
1516
1517
1518
1519
1520
1521
1522
1523

Figure 7. IFN- γ signaling in senescent tumor cells is necessary for immune surveillance

A, *Ifngr1* knockout (KO) of both proliferating and senescent NSP cells validated by flow cytometry.

B, Tumor regression phenotype of *Ifngr1* KO or control sgRNA-transfected tumor cells orthotopically injected into Bl/6N mice upon p53 restoration. A control sgRNA targeting a gene desert located on Chr8 (Ctrl KO) serves as a control.

C, Tumor regression phenotype of parental NSP tumor cells orthotopically injected into WT or *Ifng* KO mice upon p53 restoration.

D, Representative macroscopic images of tumor collected at day 21 after p53 restoration from (C).

E, Flow cytometry analysis of CD45 abundance in tumor from indicated groups.

F, Representative immunofluorescence in p53-suppressed (proliferating) and p53-restored (senescent, 7 days after p53 restoration) tumor from the indicated host.

NSP tumor cells were transduced with GFP-expressing vector for visualization. Scale bar, 50 μ m

Data is presented as mean \pm s.e.m. Two-tailed student t-test is used. *p < 0.05; **p < 0.01; ***p < 0.001.

Fig. 1. A p53-restorable tumor model to study senescence immune surveillance

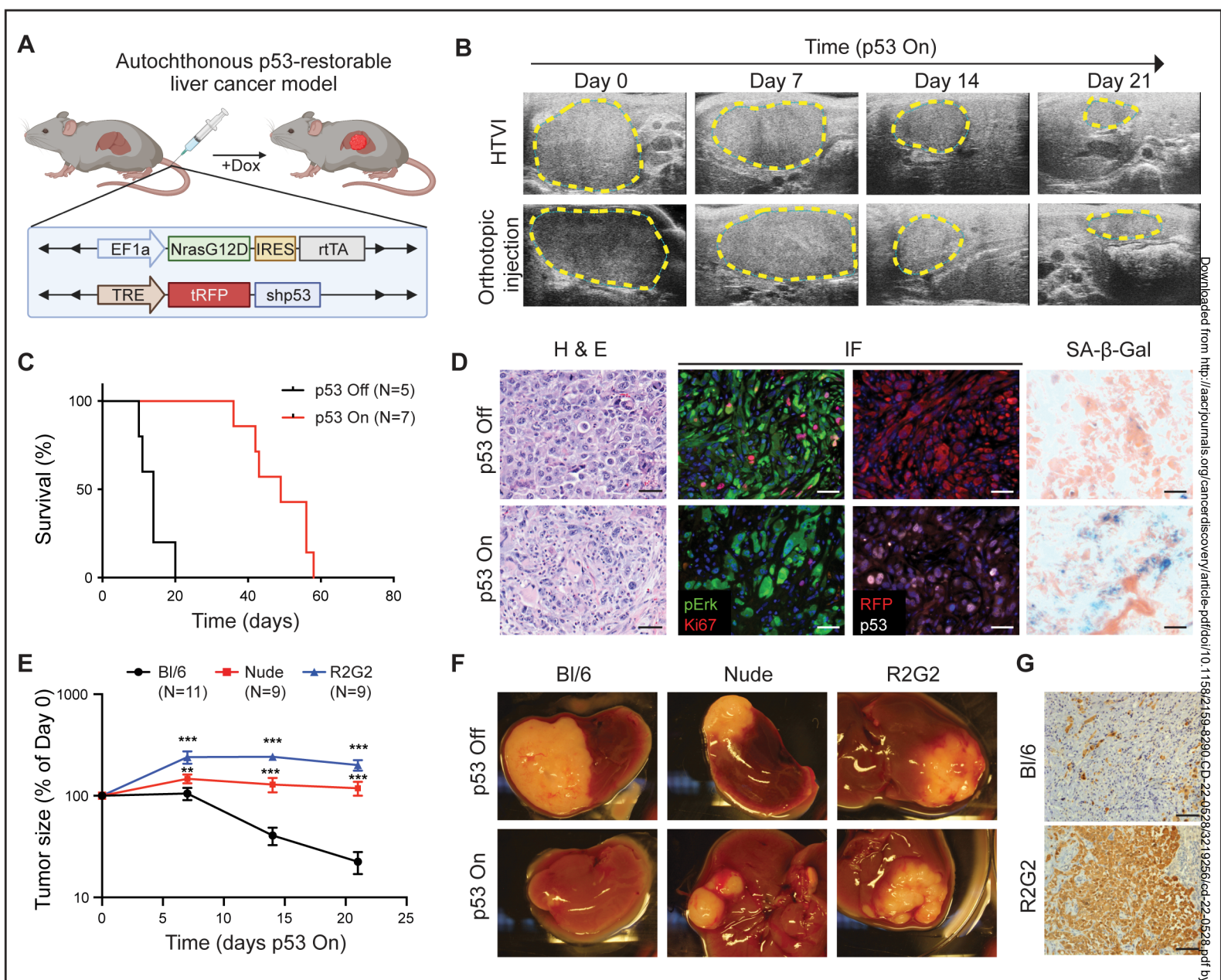


Figure 2. Senescence triggers an immune evasion-to-immune recognition tumor switch

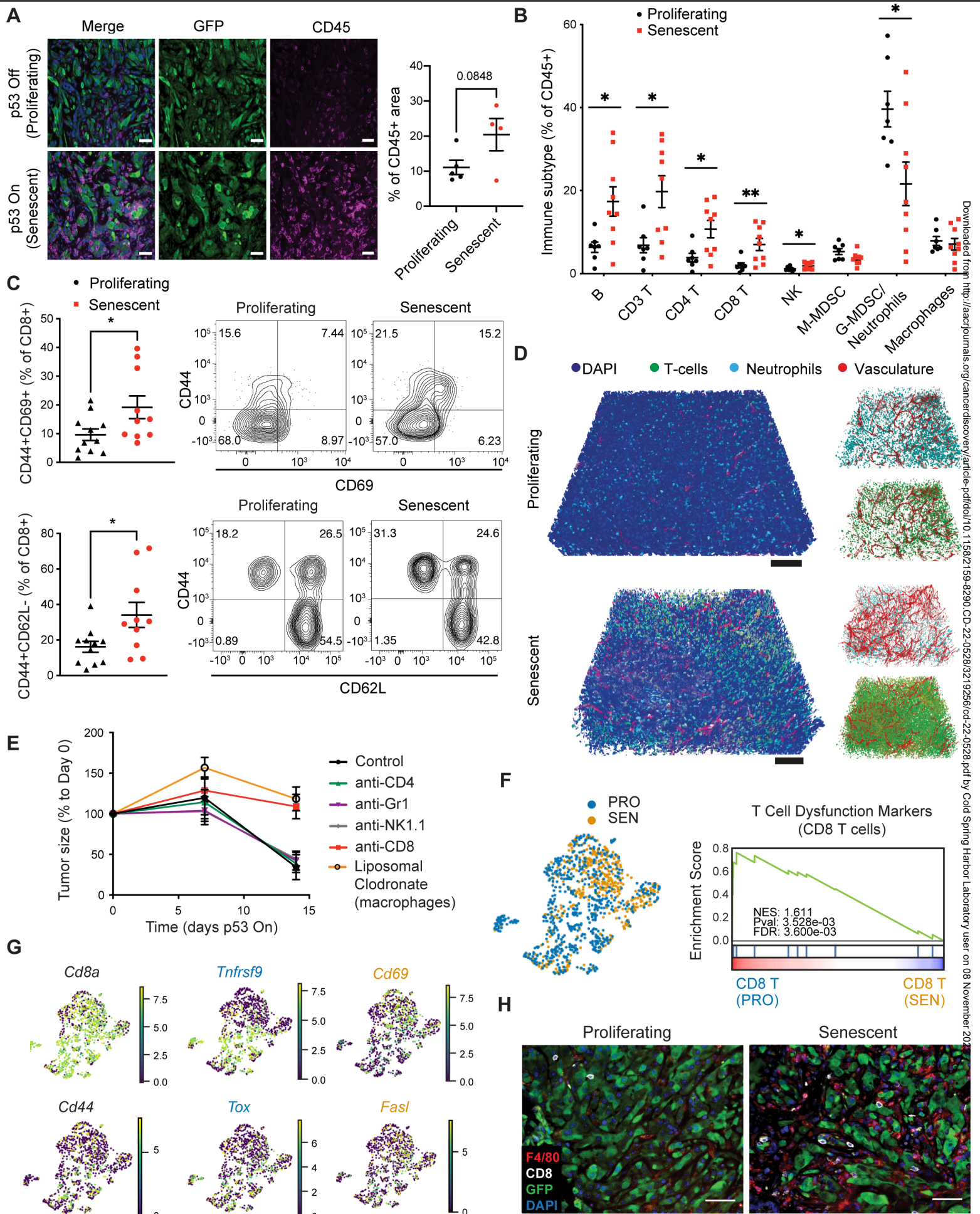


Figure 3. Senescence remodels tissue sensing programs and cell-surfaceome landscape

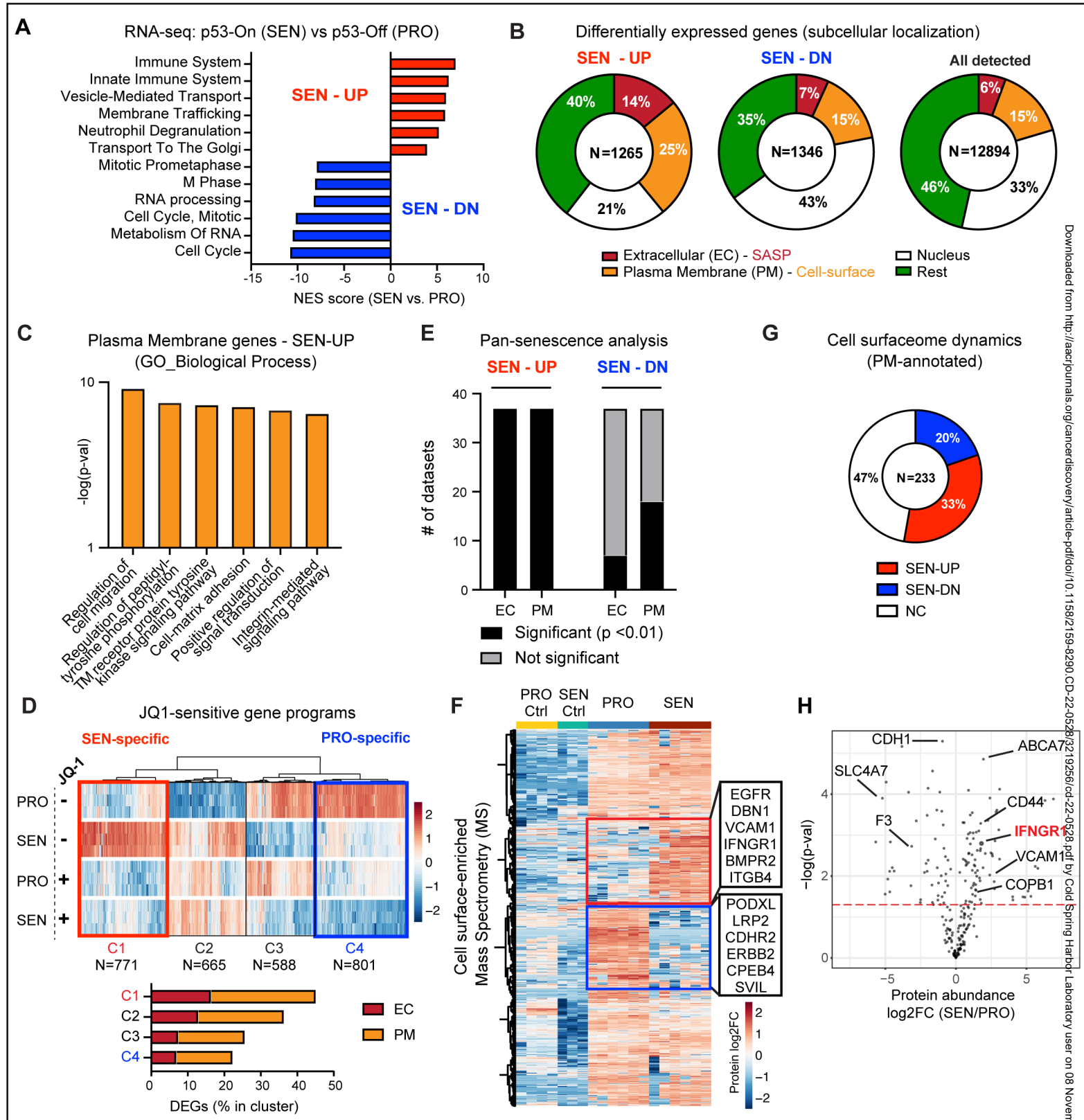


Figure 4. Senescent cells are primed to sense and amplify IFN- γ signaling

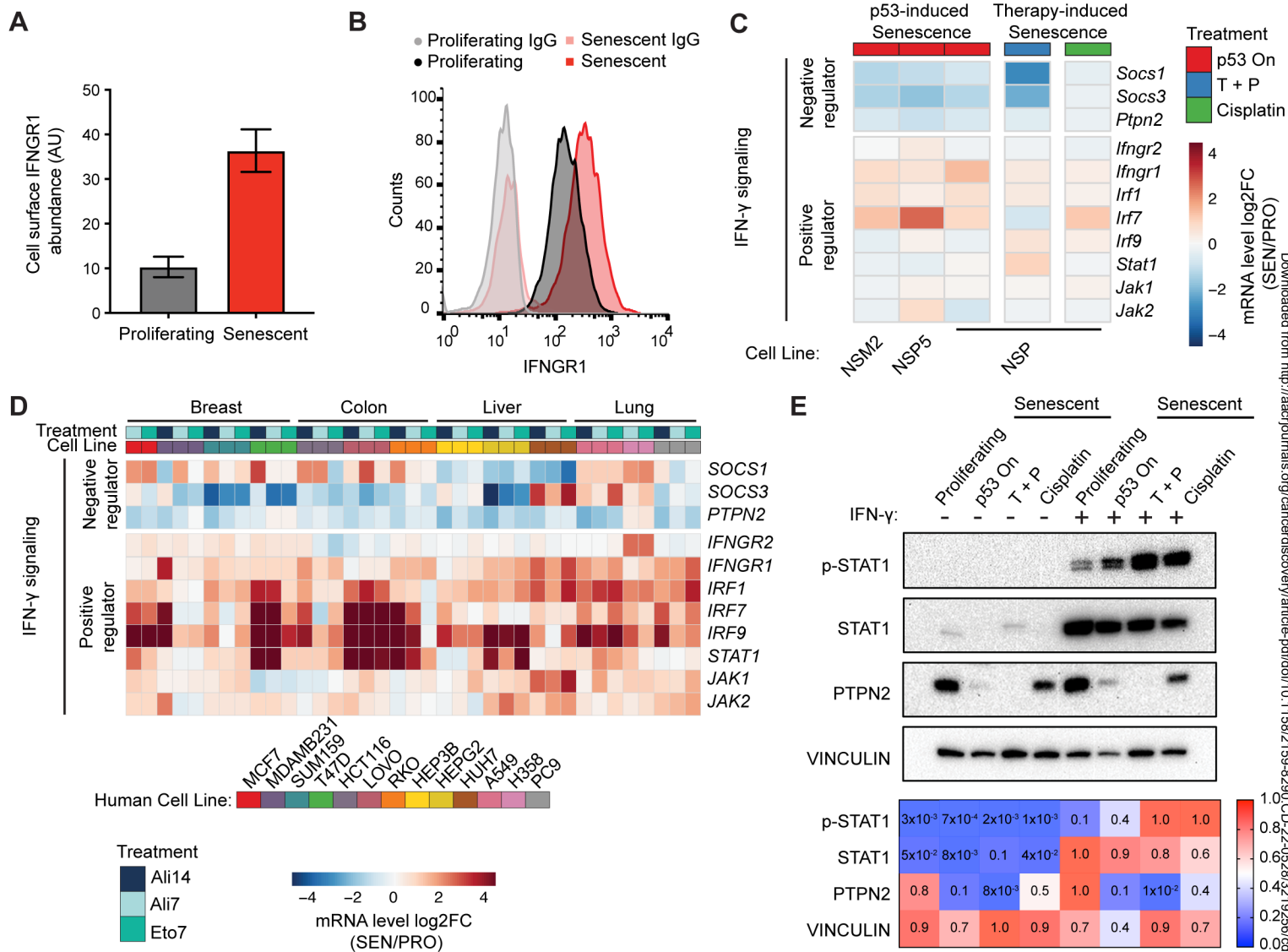


Figure 5. Senescence and extracellular IFN- γ cooperate to upregulate antigen processing and presentation machinery

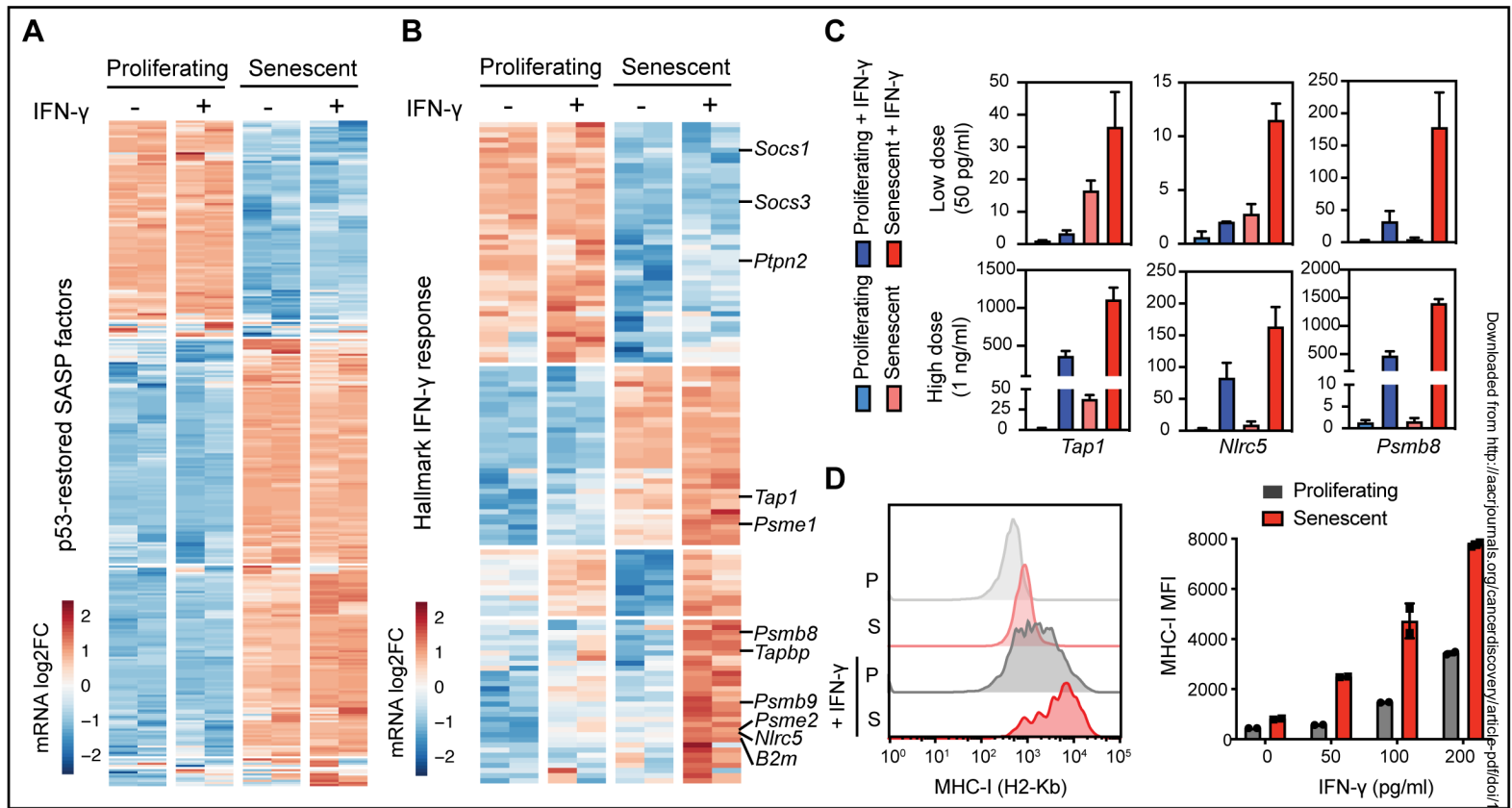


Figure 6. Senescence enhances IFN- γ -mediated heterotypic signaling from activated immune cells to tumor cells

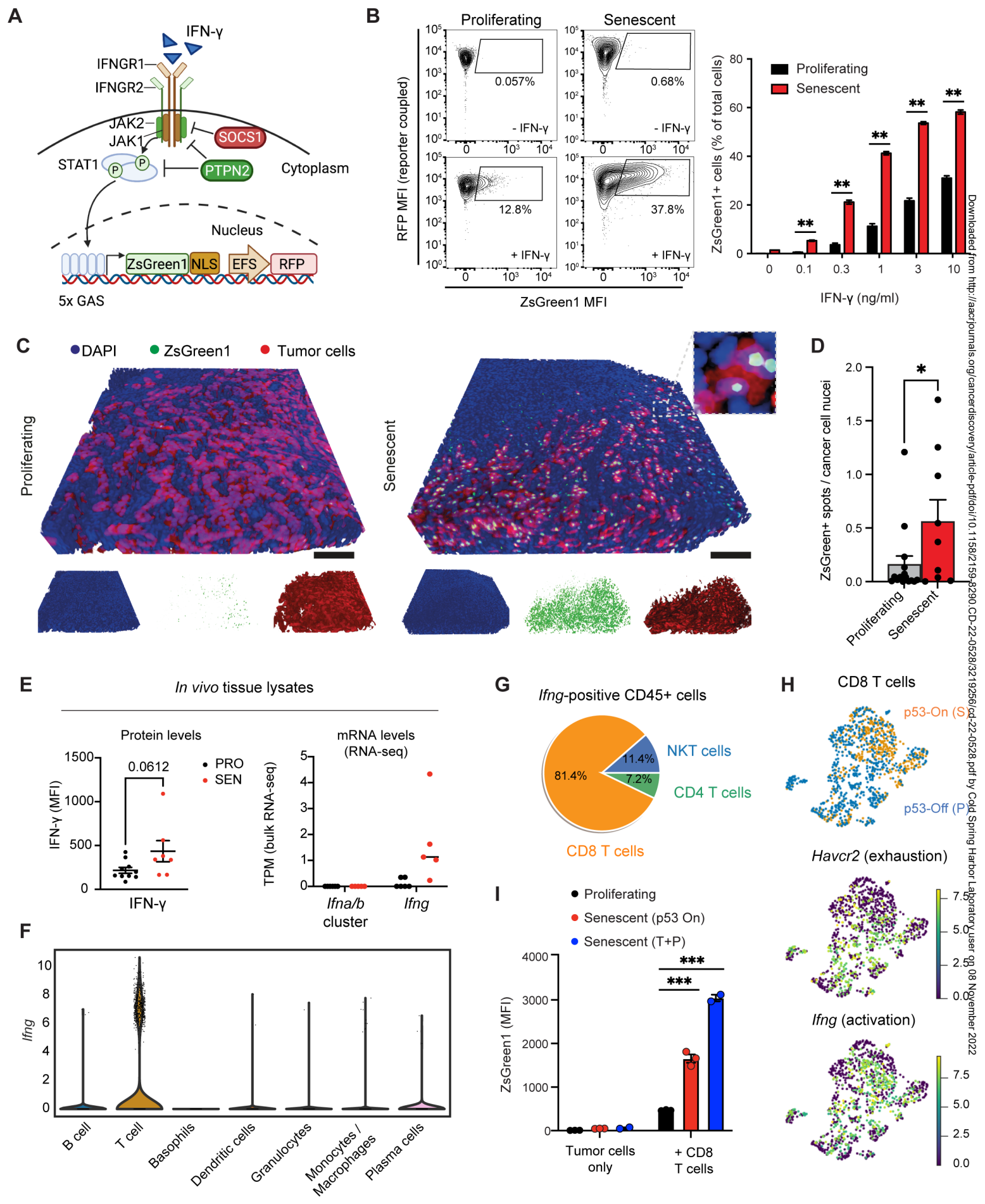


Figure 7. IFN- γ signaling in senescent tumor cells is necessary for immune surveillance

